CELLULAR NEUROSCIENCE

Neuronal metabolic rewiring promotes resilience to neurodegeneration caused by mitochondrial dysfunction

E. Motori[1]*†, I. Atanassov[2], S. M. V. Kochan[3], K. Folz-Donahue[4], V. Sakthivelu[3], P. Giavalisco[5], N. Toni[6], J. Puyal[7], N.-G. Larsson[1,8,9†]

Neurodegeneration in mitochondrial disorders is considered irreversible because of limited metabolic plasticity in neurons, yet the cell-autonomous implications of mitochondrial dysfunction for neuronal metabolism in vivo are poorly understood. Here, we profiled the cell-specific proteome of Purkinje neurons undergoing progressive OXPHOS deficiency caused by disrupted mitochondrial fusion dynamics. We found that mitochondrial dysfunction triggers a profound rewiring of the proteomic landscape, culminating in the sequential activation of precise metabolic programs preceding cell death. Unexpectedly, we identified a marked induction of pyruvate carboxylase (PCx) and other anaplerotic enzymes involved in replenishing tricarboxylic acid cycle intermediates. Suppression of PCx aggravated oxidative stress and neurodegeneration, showing that anaplerosis is protective in OXPHOS-deficient neurons. Restoration of mitochondrial fusion in end-stage degenerating neurons fully reversed these metabolic hallmarks, thereby preventing cell death. Our findings identify a previously unappreciated pathway conferring resilience to mitochondrial dysfunction and show that neurodegeneration can be reversed even at advanced disease stages.

INTRODUCTION

The central role of mitochondria in sustaining neuronal energy metabolism is emphasized by the wide spectrum of neurological symptoms associated with mitochondrial diseases in humans. Most of these diseases are caused either by mutations in genes regulating mitochondrial gene expression (*1*, *2*) or by disruption of genes involved in mitochondrial dynamics, which indirectly affect mitochondrial DNA (mtDNA) stability (*3*, *4*). Work in animal models has revealed an activation of conserved metabolic pathways in response to mitochondrial dysfunction within peripheral tissues (*5*–*7*), providing key insights into the pathogenic mechanisms underlying these complex disorders. In marked contrast, our understanding of the cell type–specific metabolic changes caused by a general failure in mitochondrial adenosine triphosphate (ATP) production in the brain is rudimentary (*8*), underscoring the need to identify therapeutic targets that may be exploited to prevent or arrest neurodegeneration (*9*). Adding to this paucity of information is the fact that nerve cells are widely held to have very limited metabolic flexibility in comparison to cell types of peripheral tissues (*10*). The capability to adapt cellular metabolism to challenging conditions in brain tissue has been confined almost exclusively to glia, given the central function of these cells in coordinating metabolite supply to neurons for fueling synaptic transmission and in reacting to injury and disease conditions (*11*–*14*). Moreover, the intrinsic cellular heterogeneity of brain tissue has hampered, to a large extent, the investigation of metabolic alterations taking place in specific neuronal subsets. As a result, the exact cellular and metabolic consequences of mitochondrial dysfunction in neurons are poorly understood.

To gain insights into the metabolic consequences underlying mitochondrial dysfunction, we isolated Purkinje neurons (PNs) at different stages of neurodegeneration caused by disruption of mitofusin 2 (*Mfn2*), which controls mitochondrial outer membrane fusion. While *Mfn2* mutations in humans are associated with a form of hereditary motor-sensory neuropathy denoted as Charcot-Marie-Tooth type 2A (*15*), conditional disruption of *Mfn2* in mice is a well-established approach to induce oxidative phosphorylation (OXPHOS) dysfunction in various neuronal subtypes (*16*–*19*), and the resulting neurodegenerative phenotypes are accompanied by progressive neurological symptoms, such as impaired locomotion (*18*, *19*) or cerebellar ataxia (*16*). By using a combination of label-free quantitative (LFQ) proteomics, metabolomics, imaging, and viral approaches, we show that progressive neurodegeneration strongly induces the expression of pyruvate carboxylase (PCx) and other enzymes involved in anaplerosis in PNs in vivo. To validate the relevance of this finding, we specifically down-regulated PCx expression in Mfn2-deficient PNs and found that this manipulation exacerbates oxidative stress and accelerates neurodegeneration, thus demonstrating that anaplerosis confers metabolic resilience to cell death. End-stage degenerating PNs with severe OXPHOS deficiency, profound mtDNA depletion, and a markedly fragmented mitochondrial network were fully rescued by reexpression of MFN2, further emphasizing that this form of neurodegeneration can be reverted even at advanced disease stages preceding cell death.

RESULTS

Proteomics of PNs identify distinct metabolic signatures induced by mitochondrial dysfunction

To visualize mitochondria in PNs with *Mfn2* knockout, we took advantage of a mouse line allowing Cre-dependent expression of

[1]Department of Mitochondrial Biology, Max Planck Institute for Biology of Ageing, 50931 Cologne, Germany. [2]Proteomics Core Facility, Max Planck Institute for Biology of Ageing, 50931 Cologne, Germany. [3]Cologne Excellence Cluster on Cellular Stress Responses in Aging-Associated Diseases (CECAD), 50931 Cologne, Germany. [4]FACS & Imaging Core Facility, Max Planck Institute for Biology of Ageing, 50931 Cologne, Germany. [5]Metabolomics Core Facility, Max Planck Institute for Biology of Ageing, 50931 Cologne, Germany. [6]Center for Psychiatric Neurosciences, Department of Psychiatry, Lausanne University Hospital, Lausanne University, Lausanne, Switzerland. [7]Department of Fundamental Neurosciences, University of Lausanne, 1005 Lausanne, Switzerland. [8]Department of Medical Biochemistry and Biophysics, Karolinska Institutet, 171 77 Stockholm, Sweden. [9]Max Planck Institute for Biology of Ageing–Karolinska Institutet Laboratory, Karolinska Institutet, Stockholm, Sweden.
*Present address: Cologne Excellence Cluster on Cellular Stress Responses in Aging-Associated Diseases (CECAD), 50931 Cologne, Germany.
†Corresponding author. Email: elisa.motori@age.mpg.de, elisa.motori@uk-koeln.de (E.M.); nils-goran.larsson@ki.se (N.-G.L.)

mitochondrial-targeted yellow fluorescent protein (YFP) (mtYFP) (*20*) and examined mitochondrial morphology in vivo. We found that disruption of the *Mfn2* gene in PNs causes a progressive fragmentation of the mitochondrial network (fig. S1A), with the earliest alterations detected already at 3 weeks of age. In contrast, substantial degeneration of the PN cell layer, as manifested by loss of calbindin immunostaining, did not start until 12 weeks of age (Fig. 1, A and B). This temporal mismatch between the earliest alterations in mitochondrial morphology and the visible onset of neuronal death prompted us to investigate the metabolic changes triggered by mitochondrial dysfunction in the period preceding cell death. We developed a fluorescence-activated cell sorting (FACS)–based strategy to isolate YFP-expressing (YFP+) PNs (Fig. 1C) and identified a small yet distinct YFP+ cell population in control mice (*Mfn2* $^{+/loxP}$::mtYFP $^{loxP\text{-}stop\text{-}loxP}$::*L7-cre*), hereafter denoted as CTRL (fig. S1B). Optimization of the gating strategy based on the relative intensity of the YFP signal enabled us to purify YFP+ somata of PNs (YFP^{high}), with a minimal contamination from non-PNs (YFP^{neg}) (fig. S1B) or putative fluorescent axonal/dendritic debris (YFP^{low}; fig. S1D, left), as confirmed by confocal microscopy (fig. S1D, right). To validate the identity of the sorted populations, we performed LFQ proteomics followed by principal components analysis and found a clear segregation between YFP^{high} and YFP^{neg} cells (fig. S1C). YFP^{high} cells showed a net enrichment for known markers of PNs (i.e., Calb1, Pcp2, Grid2, and Itpr3) (*21*, *22*), whereas proteins expressed ubiquitously in neurons or other cell types were not enriched (Fig. 1D). Intersample comparison in sorted YFP^{high} cells collected in independent experiments revealed a correlation coefficient >0.9, thus documenting a good reproducibility between biological replicates (fig. S1E). Together, these data validate our protocol for acute and specific isolation of viable PNs. Because the used L7-cre driver line induces mosaic recombination during the first postnatal week (*23*), we started to collect neurons from CTRL and conditional knockout mice (*Mfn2* $^{loxP/loxP}$::mtYFP $^{loxP\text{-}stop\text{-}loxP}$::*L7-cre*), hereafter denoted as Mfn2cKO, at 4 weeks of age when recombination is completed. As an end point, we chose the age of 8 weeks when the PN layer is still intact despite a marked mitochondrial fragmentation (Fig. 1B and fig. S1A). Overall, we quantified a total of 3013 proteins, ~22% of which annotated as mitochondrial based on MitoCarta 2.0, a widely used inventory of the mammalian mitochondrial proteome (Fig. 1E) (*24*). Differential gene expression analysis at 8 weeks indicated that only 10.5% of all proteins were significantly changed (Fig. 1F and fig. S1F), whereof 195 proteins were down-regulated and 120 were up-regulated (Fig. 1F). Notably, Ingenuity Pathway Analysis of this dataset revealed that the differentially expressed genes mostly belonged to a restricted set of specific metabolic pathways (Fig. 1G). Intriguingly, while down-regulation of pathways associated to OXPHOS and calcium signaling confirmed the induction of mitochondrial dysfunction in fusion-deficient PNs, additional categories involving mostly amino acid metabolism were significantly up-regulated, consistent with a metabolic rewiring taking place in PNs with mitochondrial dysfunction.

PNs exhibit near-normal electrophysiological responses despite mtDNA depletion and profound OXPHOS dysfunction

The proteomic data revealed a progressive decrease in the expression of proteins of complexes I, III, and IV, which all contain essential mtDNA-encoded subunits, whereas the exclusively nucleus-encoded complex II was essentially unaffected (Fig. 2A and fig. S2A). Consistent with the proteomics results, immunohistochemistry of cerebellar tissue sections revealed a progressive reduction of levels of the MTCO1 (mitochondrial cytochrome c oxidase subunit 1) subunit of complex IV in PNs (Fig. 2B). The mtDNA-encoded subunit Mtatp8 was markedly decreased (fig. S2A), whereas the steady-state levels of the nuclear-encoded ATP synthase subunits remained unchanged, consistent with the known formation of a stable subassembled F_1 complex of ATP synthase when mtDNA expression is disrupted (*7*). Assessment of mtDNA levels by real-time polymerase chain reaction (qPCR) in sorted Mfn2cKO PNs confirmed a progressive reduction of mtDNA copy number with only ~20% of mtDNA levels remaining at the age of 8 weeks compared to controls (Fig. 2C). In agreement with these results, confocal microscopy of Mfn2cKO PNs stained to detect DNA showed a time-dependent depletion of mitochondrial nucleoids (Fig. 2D). We found an up-regulation of only some of the candidates involved in mitochondrial protein degradation and stress responses, including Lonp1, Afg3l2, and Clpx, as well as of OXPHOS complex assembly factors. No overt changes in levels of proteins involved in apoptosis were detected (fig. S2B). Likewise, we found only minor changes in mitochondrial and endoplasmic reticulum channels involved in calcium transport (fig. S2C). Moreover, assessment of proteins associated with autophagy revealed no significant changes, consistent with lack of any visible induction of autophagosomes via both immunohistochemistry and electron microscopy in vivo (fig. S3). However, the progressive OXPHOS dysfunction in PNs was accompanied by marked ultrastructural mitochondrial changes. Clusters of enlarged mitochondria with profoundly altered inner membrane architecture were seen in the cell body and dendritic tree of 5- and 8-week-old Mfn2cKO PNs (fig. S4, A and B). Consistent with these ultrastructural changes and with the marked reduction in mtDNA, analysis of acute brain cerebellar slices with tetramethylrhodamine methyl ester (TMRM) revealed a significant drop in mitochondrial membrane potential in Mfn2cKO PNs (fig. S4C).

The marked OXPHOS impairment detected in 8-week-old Mfn2cKO PNs argues for a severe dysfunction in neuronal physiology. We therefore analyzed the passive electrical properties of OXPHOS-deficient neurons at 4 to 5 and 7 to 8 weeks of age by performing whole-cell patch-clamp recordings in acute cerebellar slices (Fig. 2E). Unexpectedly, the mean resting membrane potential and input resistance of Mfn2cKO neurons were similar to controls, although there was a slight variability between cells (Table 1). Also, no significant changes were detected with respect to the current-voltage relationship (*I-V* curve) at 4 to 5 weeks of age (Fig. 2F). However, no 7- to 8-week-old Mfn2cKO neuron survived the *I-V* protocol (hyperpolarizing steps), suggesting that a marked sensitivity toward hyperpolarized potentials developed at this late stage. In contrast, depolarizing currents eliciting repetitive action potential (AP) discharges were well tolerated in Mfn2cKO neurons, revealing that their overall firing pattern was not significantly different from that of control neurons at 8 weeks of age (Table 1 and Fig. 2G). Likewise, both the frequency and amplitude of spontaneous postsynaptic currents (sPSCs) were comparable to controls and exhibited a similar increase in the frequency of events from 4 to 5 to 7 to 8 weeks (Fig. 2, H and I), which is the period when synaptic maturation is being completed in PNs (*25*). Similar results were obtained following perforated patch of PNs, a configuration that prevents the possible

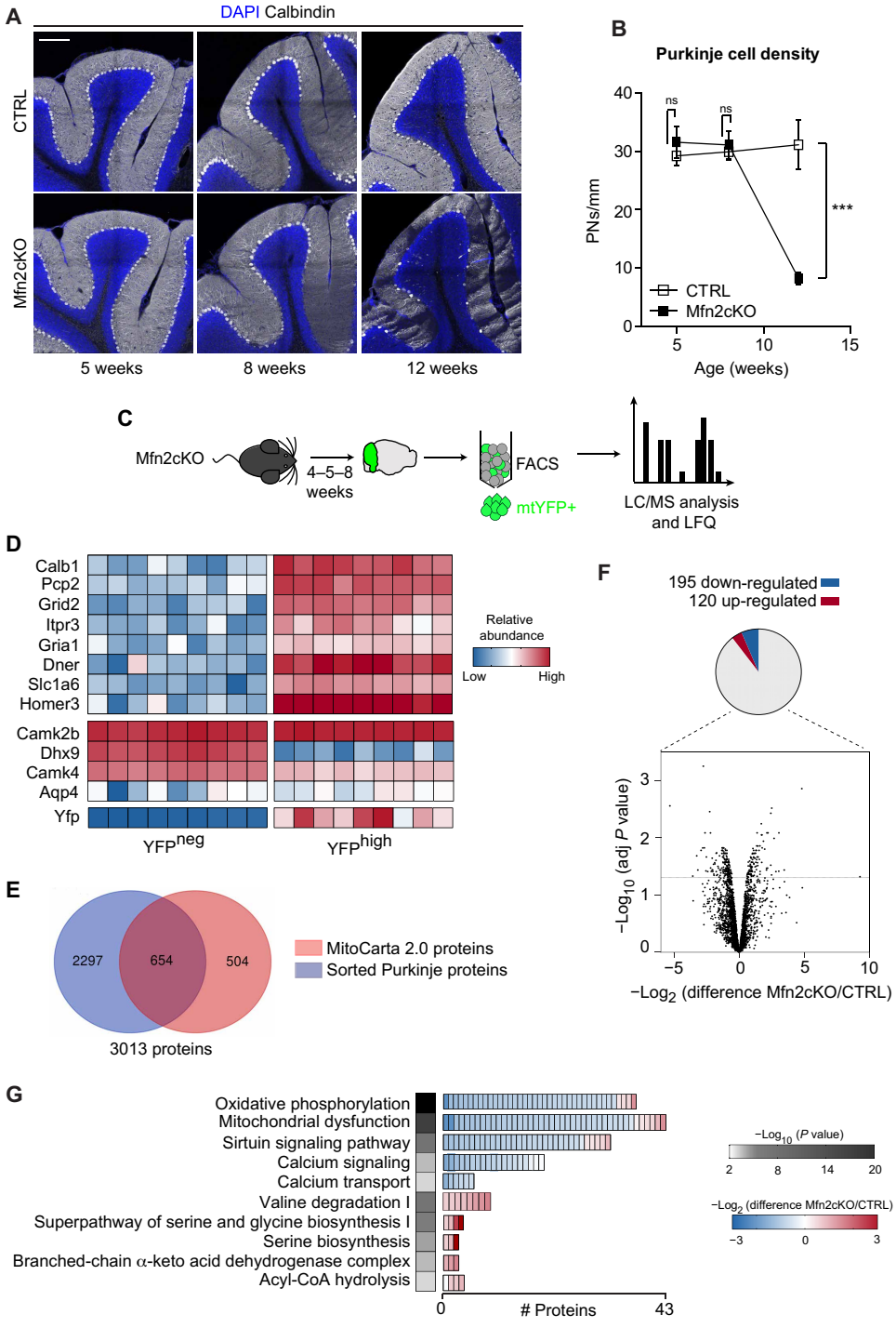

Fig. 1. Proteomics analysis identifies distinct neuronal metabolic signatures upon mitochondrial dysfunction. (**A**) Representative confocal pictures of cerebellar sections of CTRL and Mfn2cKO mice, showing the progressive loss of PNs (calbindin, gray); nuclei are counterstained with DAPI. (**B**) Quantification from (A) (one-way ANOVA, ***$P < 0.001$; $n = 4$ to 6 loops from three mice). (**C**) Experimental workflow. (**D**) Heatmap distribution of markers specific for Purkinje (top) and other cell types (middle). (**E**) Venn diagram showing the number of mitochondrial proteins identified in sorted PNs. (**F**) Volcano plot of differentially expressed proteins in Mfn2cKO neurons at 8 weeks (significance cutoff at 1.3). (**G**) Ingenuity Pathway Analysis showing the five most significant up-regulated (red) and down-regulated (blue) pathways in sorted 8-week-old Mfn2cKO PNs. The average expression level of each detected protein is shown. Grayscale heatmap: adjusted *P* value. ns, not significant.

compensation of cellular ATP deficits as could occur during whole-cell patch-clamp recordings. In particular, resting membrane potential and spontaneous firing frequency were unaffected in Mfn2cKO neurons (Fig. 2, J and K). Together, these results show that PNs with pronounced OXPHOS dysfunction can cope unexpectedly well with high-frequency firing patterns, suggesting the existence of compensatory mechanisms, allowing them to maintain near-normal electrophysiological responses.

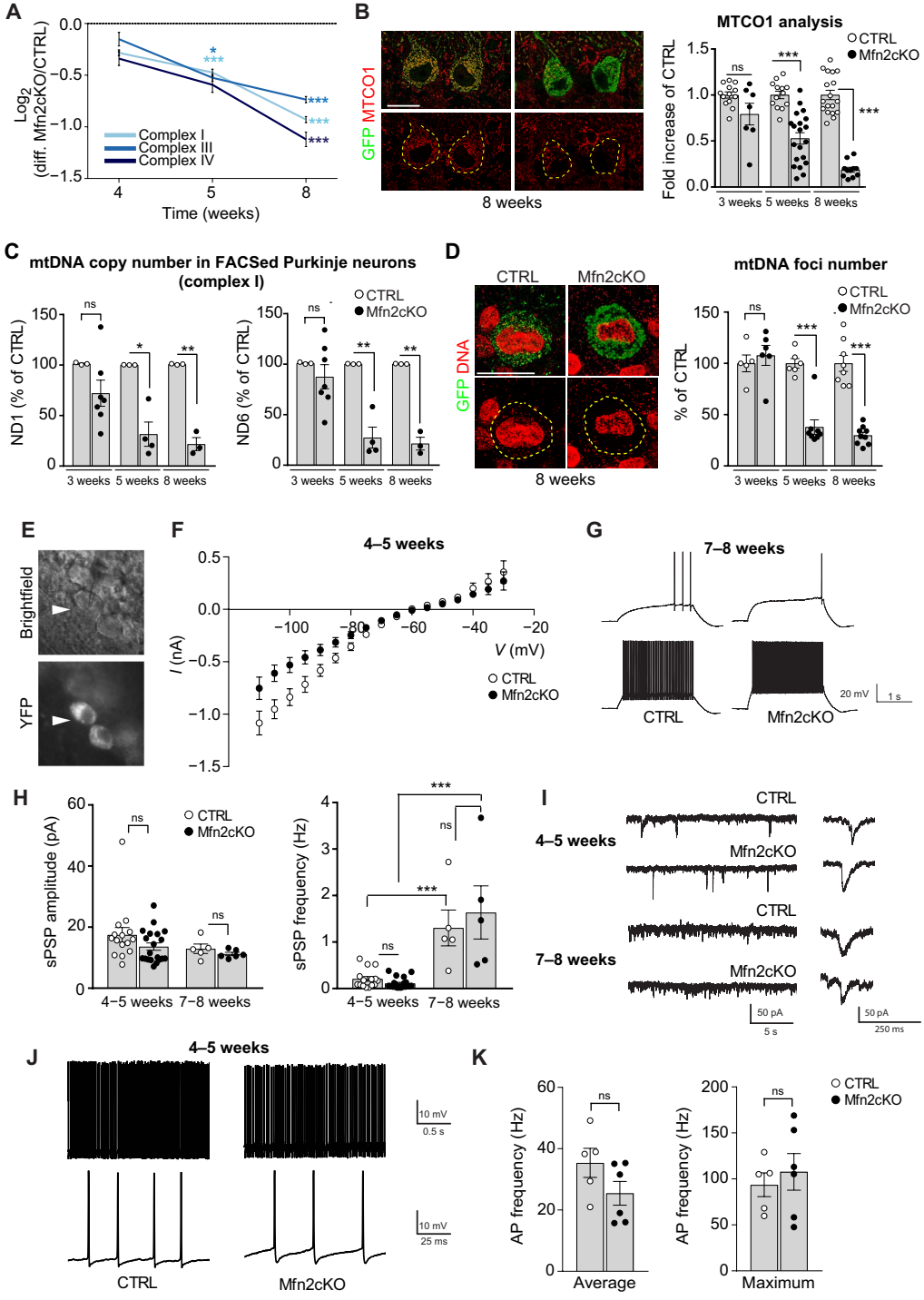

Fig. 2. PNs exhibit near-normal electrophysiological responses despite pronounced mtDNA depletion and OXPHOS dysfunction. (**A**) Time-course analysis of expression levels of OXPHOS complexes. Only proteins with $P < 0.05$ at 8 weeks were considered (two-way ANOVA). Dashed line: no regulation compared to CTRL. (**B**) Left: examples of cerebellar sections labeled with an anti-MTCO1 antibody (scale bar, 20 μm). The area occupied by Purkinje cell bodies is masked in yellow. Right: quantification of MTCO1 levels (one-way ANOVA; $n = 7$ to 20 cells analyzed from three mice). (**C**) qPCR analysis of mtDNA copy number in sorted PNs (one-way ANOVA; $n = 3$ to 7 mice). (**D**) Left: examples of cerebellar sections labeled with an anti-DNA antibody (scale bar, 20 μm). The area occupied by Purkinje cell bodies is masked in yellow. Right: quantification of mtDNA foci (one-way ANOVA; $n = 5$ to 9 cells from three mice). (**E**) Example of an acute cerebellar slice showing mitoYFP+ Purkinje cells (arrowheads) during the whole-cell patch-clamp recording. (**F**) Quantification of *I-V* curves. (**G**) Representative recordings of depolarizing current injections in CTRL and Mfn2cKO Purkinje cells. Top traces: first pulse that elicited APs. Bottom traces: maximal AP frequency. (**H**) Quantification of spontaneous post-synaptic inputs (sPSPs). Representative recording traces and their zooms are shown in (**I**). One-way ANOVA; $n = 5$ to 20 cells analyzed from three mice. Data are presented as means ± SEM; $^{*}P < 0.05$; $^{**}P < 0.01$; $^{***}P < 0.001$. (**J**) Representative traces of spontaneous APs recorded using the perforated patch-clamp modality. Top traces: maximal AP frequency. Bottom traces: zoom of single APs. (**K**) Quantification of average and maximum AP frequency from (J). Mann-Whitney test; $n = 5$ cells analyzed from four mice. Data are presented as means ± SEM; not significant.

Table 1. Electrophysiological characterization of PNs from control and Mfn2cKO mice. Data are presented as means ± SEM (one-way ANOVA, Holm-Sidak's multiple comparison test; *$P < 0.05$). The cell number is indicated in parentheses.

Property	CTRL 4–5 weeks	Mfn2cKO 4–5 weeks	CTRL 7–8 weeks	Mfn2cKO 7–8 weeks
E_M (mV ± SEM)	−59.88 ± 1.164 (25)	−56.47 ± 1.394 (20)	−63.86 ± 0.3291 (14)	−57.38 ± 1.822 (8)*
Input resistance (megohms ± SEM)	621 ± 80.46 (20)	626.2 ± 54.11 (20)	839.3 ± 88.66 (11)	628.3 ± 97.64 (7)
AP threshold (mV ± SEM)	−29.31 ± 2.602 (5)	−30.66 ± 1.305 (4)	−39.57 ± 1.791 (11)	−39.89 ± 5.006 (4)
Max AP (Hz ± SEM)	55.6 ± 4.82 (5)	52.25 ± 6.597 (4)	51 ± 7.332 (11)	72.75 ± 24.14 (4)

*Versus CTRL 7 to 8 weeks.

Mitochondrial dysfunction in neurons induces TCA cycle anaplerosis

We proceeded to investigate whether any of the categories in our proteomic dataset (Fig. 1G) would include pathways that could counteract the severe OXPHOS deficiency and thereby explain why the affected PNs could maintain near-normal electrophysiology (Fig. 2, E to K). The proteomics analysis revealed the marked up-regulation of enzymes involved in branched-chain amino acid (BCAA) catabolism (Fig. 3A and fig. S5A), whose end products, acetyl–coenzyme A (CoA) or succinyl-CoA, can replenish the tricarboxylic acid (TCA) cycle in anaplerosis. We found increased levels of both BCAA transaminases 1 (BCAT1) and BCAT2, which catalyze the first step in BCAA catabolism by generating glutamate from α-ketoglutarate (*26*). All of the subunits composing the branched-chain keto acid dehydrogenase (BCKD) complex, which catalyzes the subsequent and irreversible decarboxylation of the resulting BCAA carbon skeleton, were significantly up-regulated (Fig. 3A and fig. S5A). Yet, no overt changes in the amount of BCAAs themselves were detected in sorted PNs, possibly owing to an enhanced cellular uptake of these essential amino acids or utilization of other sources (glucose or lactate) to feed the TCA cycle (fig. S5B). OXPHOS-deficient PNs also showed increased glutaminolysis and transamination activity at 8 weeks of age as exemplified by the up-regulation of the mitochondrial enzymes glutaminase (GLS) and glutamine pyruvate transaminase 2 (GPT2) (Fig. 3, A and C). Notably, the up-regulation of GLS was confined to the spliced isoform glutaminase C (GLS-GAC) (approximately 4.5-fold change Mfn2cKO/CTRL, $P = 0.05$), whose specific up-regulation is observed in cancer tissue to support mitochondrial bioenergetics (*27*).

The fact that BCAA catabolism emerged as one of the key up-regulated pathways in our analysis strongly suggests that the anaplerotic flux into the TCA cycle may be altered in OXPHOS-deficient PNs. This may represent a largely unappreciated form of neuronal metabolic rewiring, which may have direct implications for sustaining neuronal physiology and, potentially, survival during severe OXPHOS dysfunction. Consistent with this hypothesis, we found up-regulation of the main anaplerotic enzyme PCx (approximately 1.5-fold change Mfn2cKO/CTRL; Fig. 3A), which catalyzes the conversion of pyruvate into oxaloacetate (*28*) and whose expression in brain tissue is thought to be exclusively confined to astrocytes (*29*, *30*). In line with the proteomics results, confocal microscopy revealed that PCx expression became markedly increased specifically in OXPHOS-deficient PNs, while PCx reactivity was predominantly confined to adjacent Bergmann glia in controls (Fig. 3B). To functionally test the role of the observed PCx up-regulation, we treated acute cerebellar slices with a [1-^{13}C] pyruvate tracer, whose isotopic label is lost when pyruvate is oxidized via pyruvate dehydrogenase (PDH) but is incorporated into TCA cycle intermediates when pyruvate is metabolized via anaplerotic reactions (Fig. 3D). Supporting our proteomic data, we observed substantial labeling from this tracer in aspartate in Mfn2cKO slices, while a moderate trend, albeit not significant, was also visible for citrate and malate (Fig. 3D).

PCx expression was also significantly up-regulated in dopamine neurons of MitoPark mice with mitochondrial dysfunction induced by dopamine neuron–specific disruption of the mitochondrial transcription factor A gene (*Tfam*) (fig. S6B) (*31*), thus showing that pyruvate anaplerosis is up-regulated during neuronal OXPHOS dysfunction in vivo. Notably, distinct enzymes potentially involved in anaplerosis, which have been proposed to be expressed in neurons (*32*–*34*), were found to be significantly up-regulated in OXPHOS-deficient PNs, e.g., the propionyl-CoA carboxylase (PCC-A), which converts propionyl-CoA into succinyl-CoA via malonyl-CoA, and the mitochondrial malic enzyme 3 (ME3), which primarily operates by recycling pyruvate from malate (Fig. 3, A and C) (*33*, *35*). In addition, we found a significant increase in the Pdk3 enzyme, which phosphorylates and thus inactivates the PDH (*36*), while no changes were detected for the Pdp1 enzyme that activates PDH or for the PDH enzyme complex itself (Fig. 3A). Consistently, phosphorylation of the pyruvate dehydrogenase E1 component subunit alpha (PDHE1α) subunit of the PDH complex at Ser^{293}, which is known to inhibit PDH enzymatic activity (*37*), was enhanced in Mfn2cKO PNs (fig. S6C), further supporting a rerouting of pyruvate to anaplerotic pathways.

Last, we found a significant up-regulation of the serine and glycine biosynthesis super-pathway, the associated mitochondrial folate (1C) cycle, and proline biosynthesis (Fig. 1G and fig. S5C), whose activation has been reported in peripheral tissues during mitochondrial dysfunction (*5*–*7*). Supporting these proteomic data, confocal analysis of cerebellar sections in 8-week-old mice revealed a marked immunoreactivity against serine hydroxymethyltransferase 2 (SHMT2) (a key enzyme of the mitochondrial folate cycle) in OXPHOS-deficient PNs (fig. S5D). The up-regulation of serine and proline biosynthesis was further substantiated by metabolic tracing experiments in acute cerebellar slices incubated with ^{13}C-U-glucose, which revealed an increased flux of carbon isotopomers into serine and proline (fig. S5E). As the reactions promoted by GLS and GPT2 are responsible for the synthesis of glutamate from glutamine and for the transamination between glutamate and α-ketoglutarate, respectively, their up-regulation suggests an increased demand for glutamate in OXPHOS-defective neurons, possibly aimed at sustaining the increased biosynthesis of proline (fig. S5C). In contrast to these changes, proteomics analyses of sorted cerebellar astrocytes from the PN-specific Mfn2cKO mice revealed that these pathways, including all anaplerotic enzymes,

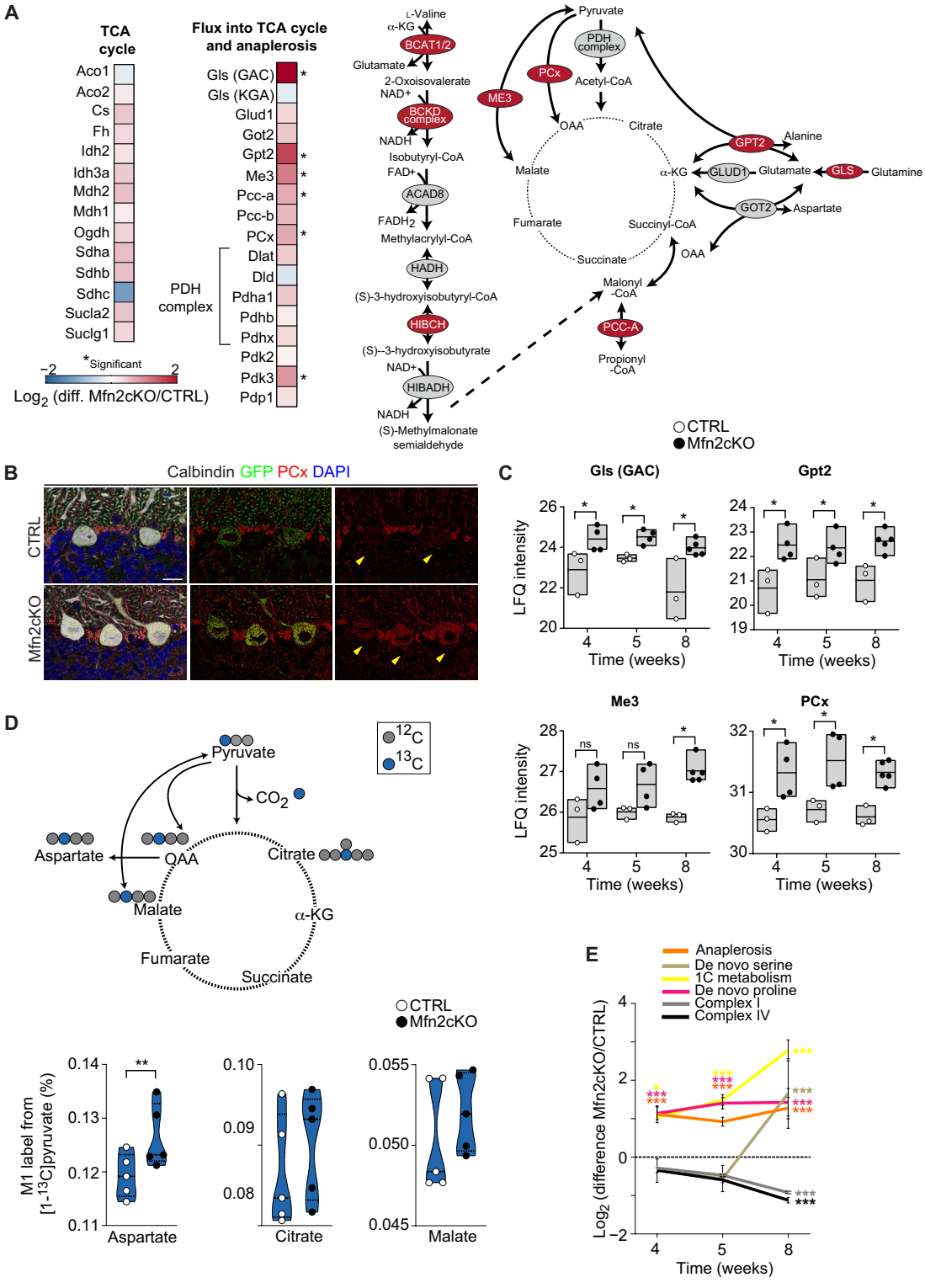

Fig. 3. Mitochondrial dysfunction in neurons induces TCA cycle anaplerosis. (**A**) Heatmap showing the fold change in protein levels of the indicated pathways at 8 weeks. (**B**) Examples of cerebellar sections labeled with an anti-PCx antibody (scale bar, 20 μm). Yellow arrowheads point to the Purkinje cell bodies. (**C**) Time-course protein expression analysis of significant candidates identified for anaplerosis (multiple *t* test, *FDR < 5%; $n = 3$ to 5 mice). (**D**) Top: Schematic representation showing the different entry modalities of the labeled carbon contained in the [1-^{13}C]pyruvate tracer (i.e., via either PDH or anaplerotic pathways). Bottom: violin plots showing the quantification of single-labeled carbon (M1) percentage into aspartate, citrate, and malate upon labeling of acute cerebellar slices with [1-^{13}C]pyruvate (paired *t* test; $^{**}P < 0.01$). (**E**) Integrated time-course analysis of the indicated pathways. Only proteins with $P < 0.05$ at 8 weeks were considered. Dashed line: no regulation (two-way ANOVA; $^{*}P < 0.05$; $^{***}P < 0.001$). Data are presented as means ± SEM.

were not significantly changed in expression, thus demonstrating the selectivity of this metabolic rewiring to degenerating PNs (fig. S6, D to G).

Together, these analyses revealed notably different patterns in the temporal activation of specific metabolic pathways in PNs. While anaplerosis and 1C remodeling are early events induced by mitochondrial dysfunction in neurons (Fig. 3E and fig. S5C) and even anticipate measurable changes in complex I and IV expression, the alterations in the de novo synthesis of serine only became manifest at late stages of OXPHOS dysfunction (Fig. 3E and fig. S5C). These findings identify a sequential program in which stress-induced mitochondrial (1C cycle) and cytosolic (serine biosynthesis) responses act in concert with an increase in TCA cycle anaplerosis to remodel neuronal metabolism.

Reversible TCA cycle anaplerosis reveals metabolic plasticity in OXPHOS-deficient neurons and confers resilience to neurodegeneration

The finding that 8-week-old OXPHOS-deficient PNs can sustain high-frequency firing activity and undergo prominent metabolic rewiring to compensate for mitochondrial dysfunction raises the intriguing possibility that these cells might be amenable to therapeutic interventions to delay or prevent neurodegeneration even at this late stage. We addressed this possibility by two independent interventions. In the first approach, we designed a Cre-dependent adeno-associated viral (AAV) vector to enable MFN2 reexpression selectively in OXPHOS-deficient PNs in vivo (fig. S7A). Validation of this AAV encoding MFN2 and the fluorescent reporter mCherry (Mfn2-AAV) in primary neuronal cultures in vitro resulted in MFN2 expression in a Cre-dependent fashion and rescued mitochondrial morphology, thereby preventing neurite degeneration in Mfn2cKO neurons (fig. S7, B, D, and E). Next, we proceeded with in vivo experiments by stereotactically delivering the Mfn2-AAV into the cerebellar cortex of Mfn2cKO and control mice at the age of 8 weeks and analyzed the mice at the age of 12 weeks (Fig. 4A), when the vast majority of PNs have died in untreated Mfn2cKO mice (Fig. 1, A and B) (*16*). Viral transduction in vivo resulted in selective expression in PNs in a few cerebellar loops (fig. S7, G and H). Injections of a control AAV only expressing mCherry (Ctrl-AAV) had no visible effect on the extent of neurodegeneration in Mfn2cKO animals. In contrast, analysis of Mfn2cKOs transduced with the Mfn2-AAV revealed a notable protective effect of the PN cell layer (Fig. 4, B and C). In particular, neuronal density appeared almost indistinguishable from control animals (Fig. 4, B and C, and fig. S7, H and I). Expression of MFN1 rather than MFN2 was equally effective in rescuing neuronal death (Fig. 4C and fig. S7, C and F), suggesting that ectopic MFN1 expression can efficiently complement lack of MFN2. Further analysis at the single-PN level revealed that Mfn2-AAV largely rescued mitochondrial ultrastructure, normalized mtDNA levels, and reversed the high expression of the anaplerotic marker PCx (Fig. 4, C to E). Visual inspection of the rescued Mfn2cKO mice during resting behavior showed an improvement in both posture and motor symptoms (movies S1 to S3). Together, these experiments demonstrate that late reintroduction of MFN2 into severely OXPHOS-deficient PNs is sufficient to reverse mtDNA depletion and the induction of anaplerosis, thereby preventing axonal degeneration and neuronal death in vivo.

Last, we investigated the importance of anaplerosis induction for cell survival in PNs experiencing OXPHOS dysfunction. We generated an mCherry-encoding AAV-shRNA (short hairpin RNA) specifically targeting the mouse PCx mRNA (AAV-shPCx) and injected this virus or its scramble control (AAV-scr) into the cerebellum of Mfn2cKO mice. Injections were performed during the fourth week of age (Fig. 5A) to achieve efficient knockdown of PCx during the period when PCx expression is increased (Fig. 3C) and the PN cell layer is still largely intact (Fig. 1A). Notably, knockdown of PCx (fig. S8A) caused a marked acceleration of PN death, which was uniquely restricted to the infected loops (Fig. 5, B and C). To gain mechanistic insights into the metabolic effects induced by PCx up-regulation, we examined the redox state of PNs following PCx knockdown and simultaneous AAV-mediated expression of the optical biosensor Grx1-roGFP2 (fig. S8, B to D), which allows assessing the relative changes in glutathione redox potential (*38*). We then performed two-photon fluorescence lifetime imaging microscopy (FLIM) in acute brain slices of 7-week-old Mfn2cKO or control littermates to probe for potential changes in cytosolic redox state after validation of FLIM conditions (fig. S8, E to G). Analysis revealed a marked increase in the oxidation state of individual Mfn2cKO PNs lacking PCx expression, in contrast to control neurons or Mfn2cKO PNs expressing only the scramble shRNA (Fig. 5, D and E). The percentage of Mfn2cKO PNs displaying a highly oxidized state more than tripled when PCx expression was down-regulated (Fig. 5E), showing that PCx up-regulation maintains the redox capacity in degenerating neurons.

In summary, the data we present here show that degenerating end-stage PNs with severe OXPHOS deficiency, profound mtDNA depletion, and very abnormal cristae morphology can be fully rescued by reexpression of MFN2, providing evidence for the reversibility of ongoing neurodegeneration even at advanced disease stages preceding cell death. This degree of metabolic flexibility is further emphasized by the capability of neurons of inducing anaplerosis, a form of TCA cycle rewiring, which plays a protective role as suppression of PCx expression in OXPHOS-deficient PNs enhances cell death (Fig. 5F).

DISCUSSION

In this study, we provide evidence that PNs respond to OXPHOS dysfunction with a metabolic program of differentially activated pathways converging onto TCA cycle anaplerosis. We corroborated the proteomic analyses by a number of complementary approaches and revealed that neurons have a previously unappreciated form of metabolic flexibility when challenged with severe mitochondrial dysfunction. To our surprise, this whole rewiring process does not necessarily mark terminal metabolic states that gradually and irreversibly accompany neurodegeneration, but our data show that it likely constitutes a compensatory mechanism to sustain neuronal function even at stages immediately preceding cell death. This finding indicates that neurons accommodate a substantial degree of metabolic plasticity in vivo, as demonstrated by the fact that late-stage reintroduction of MFN2 can reverse the expression of key metabolic hallmarks and prevents PNs from degenerating, while on the contrary, suppression of anaplerosis leads to a much accelerated neurodegeneration.

One of the most intriguing findings in our study is that OXPHOS-deficient PNs are capable of modifying the TCA cycle metabolism by up-regulating enzymes that specifically fuel anaplerosis. Metabolic rewiring is a common feature of cancer cells, and some of them specifically rely on glutamine to replenish the TCA cycle

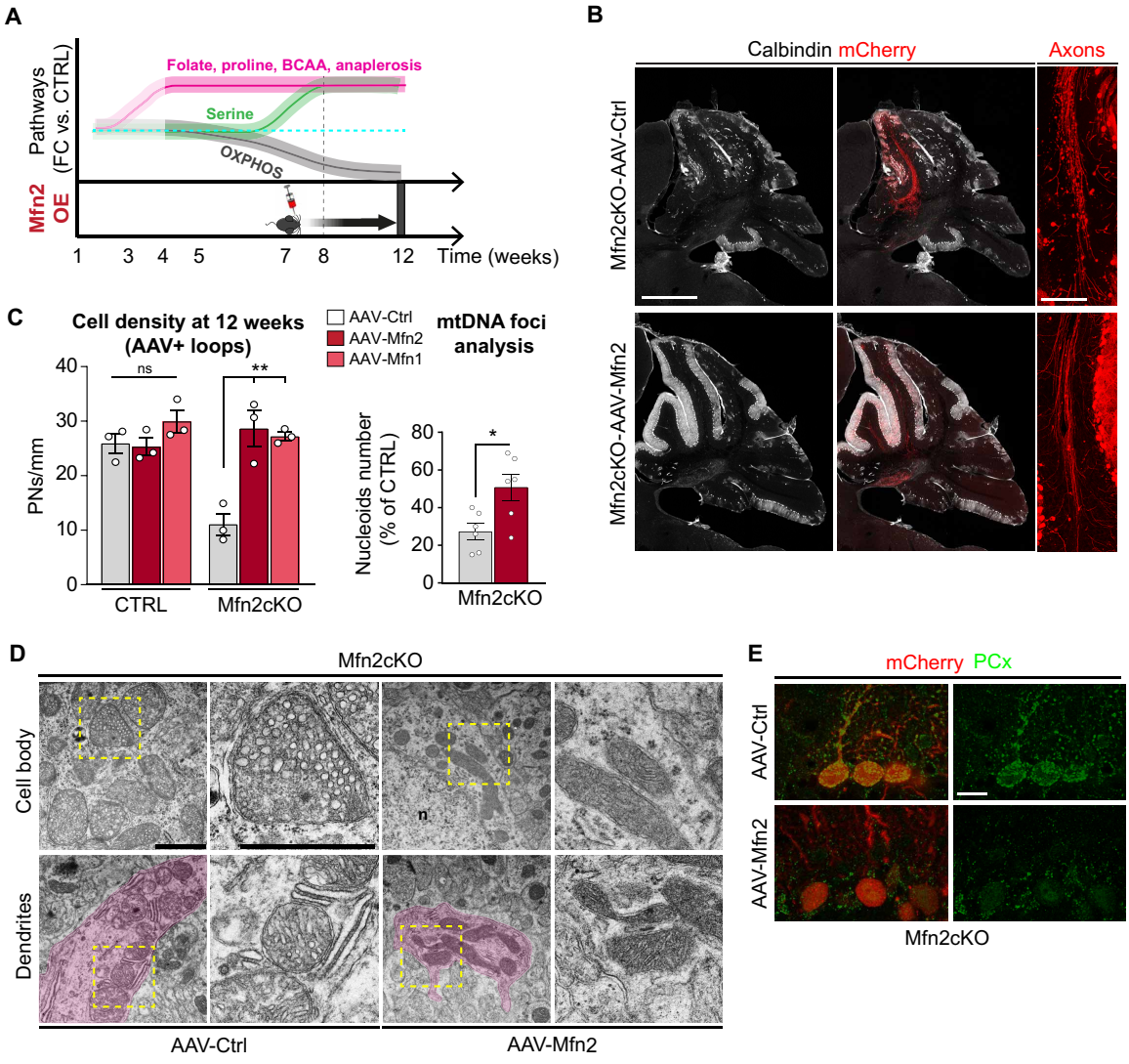

Fig. 4. Reversible TCA cycle anaplerosis reveals metabolic plasticity in OXPHOS-deficient neurons. (**A**) Scheme showing the experimental timeline to inject AAVs encoding for MFN2 when the shown metabolic pathways became activated. (**B**) Representative confocal pictures of 12-week-old cerebellar sections in Mfn2cKO mice transduced at 8 weeks and labeled with an anti-calbindin antibody. Right: zooms of the axonal fibers. Scale bars, 450 and 75 μm for the axonal zoom. (**C**) Left: Quantification of Purkinje cell density in AAV-transduced loops (AAV+) (one-way ANOVA; $n = 3$ mice). Right: mtDNA foci analysis in transduced PNs at 12 weeks (unpaired t test; $n = 6$ cells from three mice). *$P < 0.05$; **$P < 0.01$. (**D**) Representative transmission electron microscopy pictures of PNs from cerebellar sections of Mfn2cKO transduced with the indicated viral vectors. The pink mask illustrates the area occupied by the dendrites, and yellow dashed squares illustrate the zoom provided on the right; n indicates the cell nucleus. Scale bars, 1 μm. (**E**) Examples showing PCx staining in transduced PNs at 12 weeks. Scale bar, 20 μm. OE, overexpression; FC, fold change.

intermediates for producing reducing equivalents that drive the respiratory chain and sustain the generation of lipids and nucleotide biosynthetic precursors (*39*, *40*). A recent study showed that rewiring of glutamine/glutamate metabolism is a prominent feature also in peripheral tissues experiencing OXPHOS dysfunction (*5*, *41*), whereby the direction of the glutamine flux into the TCA cycle is decided according to the severity of OXPHOS impairment (*41*). Yet, unambiguous evidence for any similar extent of metabolic plasticity in neurons in vivo and its possible relevance in disease settings have been lacking. In a recent study performed in vitro, primary cortical neurons were shown to mobilize the glutamate pool reserved for neurotransmission to promote oxidative metabolism and anaplerosis under metabolic stress conditions (*42*). Conspicuously, pyruvate carboxylation has been suggested to sustain oxaloacetate synthesis in cultured cerebellar granule neurons upon pharmacological inhibition of the TCA cycle enzyme succinate dehydrogenase (*34*). However, the physiological relevance of these mechanisms for brain tissue, where anaplerosis is thought to be mainly confined to astrocytes (*43*), remains to be clarified. In this context, our data suggest that OXPHOS-impaired PNs in vivo can switch to BCAA degradation and pyruvate carboxylation as the two main sources for replenishing TCA pool intermediates. While a putative contribution of BCAA catabolism to neuronal energy metabolism beyond a role in supplying glutamate and GABA for neurotransmission has been suggested (*44*), any proof for these mechanisms in vivo has been lacking. It is thus tempting to speculate that dysfunctional PNs may compensate cell-autonomously for the depletion of TCA intermediates driven by anabolic processes by increasing anaplerosis. In particular, PCx

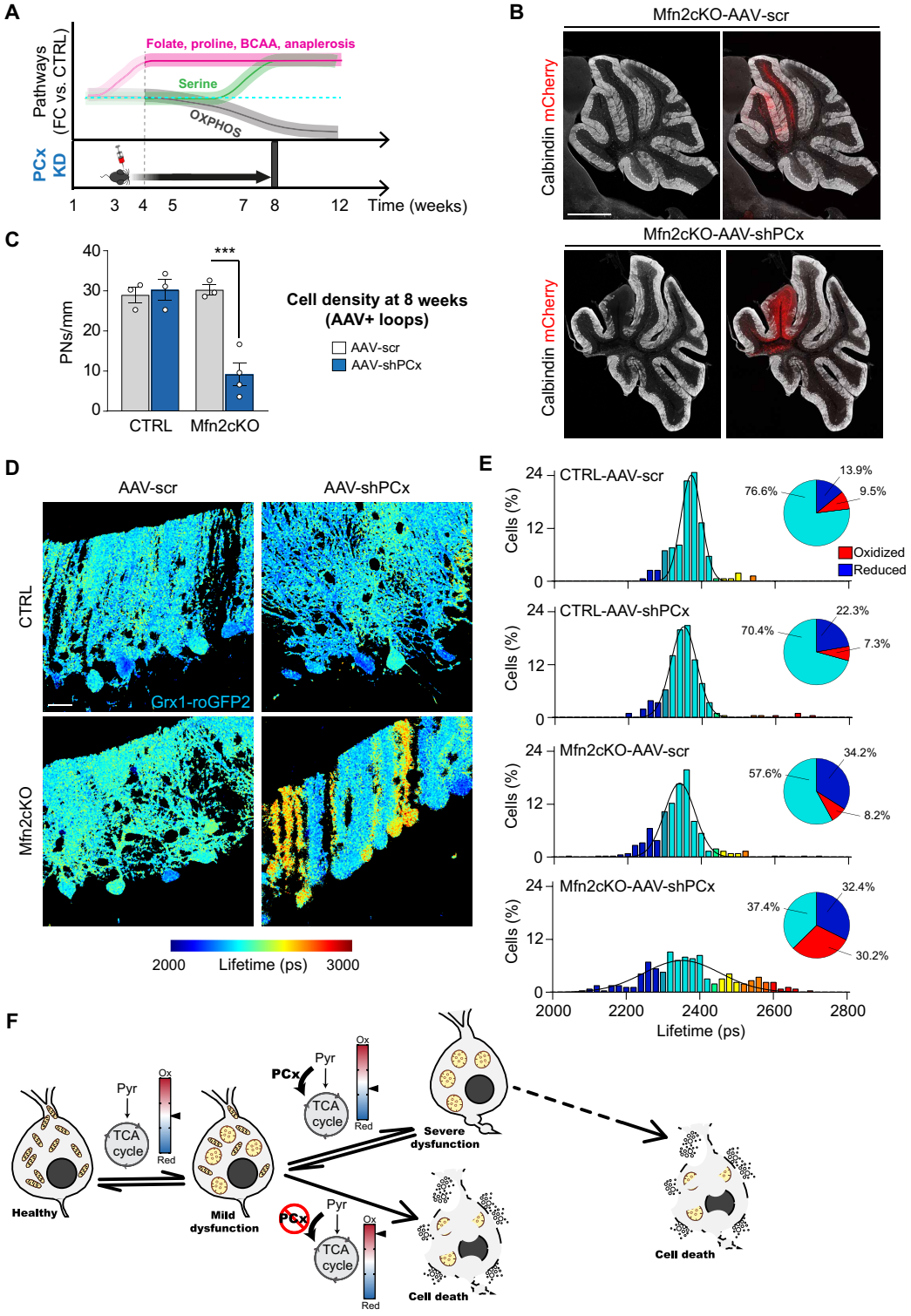

Fig. 5. Reversible TCA cycle anaplerosis confers resilience to neurodegeneration. (**A**) Scheme showing the experimental timeline to inject AAVs encoding for shPCx when the shown metabolic pathways became activated. (**B**) Representative confocal pictures of 8-week-old cerebellar sections in Mfn2cKO mice transduced at 4 weeks and labeled with the anti-calbindin antibody. Scale bar, 450 μm. (**C**) Quantification of Purkinje cell density in AAV-transduced loops (one-way ANOVA; $n = 3$ to 4 mice). Data are presented as means ± SEM; ***$P < 0.001$. (**D**) Representative FLIM pictures showing the mean lifetime of 7-week-old PNs expressing the glutathione redox sensor Grx1-roGFP2 at the indicated experimental conditions. LUT (look up table) scale: lifetime interval in picoseconds. Scale bar, 25 μm. (**E**) Histogram profile showing the distribution of Grx1-roGFP2 lifetime values from (D) ($n = 158$ to 368 cells from two mice per condition). Pie charts on top of each histogram: number of cells displaying significantly longer (red, oxidized) or shorter (blue, reduced) lifetime values, which exceeded 1 SD of the mean lifetime value in CTRL-AAV-scr. (**F**) Proposed model showing the protective role of neuronal PCx up-regulation.

up-regulation may be required to sustain an increased demand for aspartate, as suggested in proliferating cells with mitochondrial dysfunction (*45*). However, our metabolomic analysis did not disclose any significant changes in steady-state levels of aspartate in Mfn2cKO PNs (fig. S6A), presumably reflecting distinct metabolic utilization of aspartate between proliferating cells and postmitotic neurons. While the precise mechanisms underlying PCx up-regulation in dysfunctional neurons in vivo remain to be characterized, we showed that this anaplerotic reaction plays an important role in maintaining the neuronal redox state, as evidenced by FLIM experiments in cerebellar slices. In particular, preventing PNs from up-regulating PCx resulted in a more oxidized state and accelerated cell death. Activation of BCAA degradation and pyruvate carboxylation are pathways that do not characterize peripheral tissues targeted by mitochondrial dysfunction (*7*), and therefore, they appear to be a preferential, if not a unique, feature of OXPHOS-deficient neurons with important implications for neurodegeneration.

Cerebellar disorders are a heterogeneous class of neurodegenerative diseases that typically manifest with ataxia and often involve damage to PNs (*46*). This neuronal population is particularly vulnerable to mitochondrial dysfunction, as their selective degeneration in mice is sufficient to reproduce many of the motor symptoms that characterize spinocerebellar ataxia in humans (*16*, *47*, *48*). Transgenic mouse models bearing mutated genes, which are associated with human spinocerebellar ataxia, have also been reported to have mitochondrial dysfunction (*49*, *50*), emphasizing the importance of investigating the consequences of OXPHOS deficiency in PNs. For this reason, effective methods to properly isolate and study this unique neuronal population are of particular interest. However, given that PNs are very sensitive to stress and are largely underrepresented in the whole cerebellar cell population, their selective isolation as whole cells remains a challenging aspect for many omics-based studies. While absolute lack of contamination from other cell types is virtually impossible to achieve, especially from adult tissue, we combined an effective dissociation step with FACS to obtain sufficient amounts of viable neurons for downstream proteomic analysis with a reasonably high protein coverage (~3000 proteins) for a single cell population, in comparison with existing datasets from whole cerebellum (*51*). By preserving whole-cell viability, the approach we provide here allows us to examine not only changes in metabolic pathways within mitochondria but also their cytosolic counterparts, thus complementing well with recent methods that take advantage of mitochondrial membrane tags to enrich for cell type–specific populations of mitochondria from complex tissue (*52*, *53*). The method we describe not only will be relevant for studies of Purkinje cells but also can be easily adapted and used for any cell type to address metabolic alterations in the diseased brain, including in other models of mitochondrial dysfunction.

Last, we identified a therapeutic window during this metabolic rewiring process, within which key hallmarks of cellular stress can be fully reversed, and neuronal degeneration itself can be prevented. Understanding the functional implications of the rewiring described here may thus provide fundamental insights into possible therapeutic approaches to sustain neuronal viability during mitochondrial dysfunction. Future studies aiming at dissecting the changes in energy metabolism in other brain cell types are required to fully reveal the applicability of this principle to other neurological diseases.

MATERIALS AND METHODS

Mouse models

MitoPark mice were previously described (*31*). C57BL/6N mice with loxP-flanked Mfn2 genes were previously described (*18*) and crossed with L7-Cre mice (*23*). The resulting double heterozygous offspring were in turn crossed with homozygous $Mfn2^{loxP}/Mfn2^{loxP}$ mice to generate Purkinje-specific knockouts for Mfn2 ($Mfn2^{loxP}/Mfn2^{loxP}$; L7-cre). In a subset of matings, the Gt(ROSA26)SorStop-mito-YFP allele (stop-mtYFP) (*20*) was introduced via additional crossing. All animal procedures were conducted in accordance with the European, national, and institutional guidelines and were approved by the Landesamt für Natur, Umwelt und Verbraucherschutz, Nordrhein-Westfalen, Germany. Animal work also followed the guidelines of the Federation of European Laboratory Animal Science Associations.

Primary cultures of mouse cortical neurons

Mouse embryos (E13) were isolated following cervical dislocation of the anesthetized pregnant mother. Cortices were dissected in Hanks' balanced salt solution (HBSS) supplemented with 10 mM Hepes and dissociated by means of enzymatic digestion by incubating the tissue in Dulbecco's modified Eagle's medium (DMEM) containing papain (20 U/ml) and cystein (1 μg/ml) for 20 min at 37°C, followed by mechanical trituration in DMEM supplemented with 10% fetal bovine serum. Cells were plated at a density of 2×10^6 per 6-cm dishes or at a density of 0.5×10^5 cells/cm^2 on poly-L-lysine–coated glass coverslips for imaging analysis. After 4 hours, the medium was replaced with Neurobasal serum-free medium containing 1% B27 supplement and 0.5 mM GlutaMax. Neurons were then maintained at 37°C and 5% CO_2 throughout the experiment, and semi-feeding was performed once per week. For inducing recombination in vitro, neurons were treated at Day in vitro (DIV) 2 with 3 μl (24-well dishes) or 0.5 μl (24-well plate) of the following AAV9 viral vectors: AAV9.CMV.PI.eGFP.WPRE.bGH (Addgene, catalog no. 105530-AAV9) and AAV9.CMV.HI.eGFP-Cre.WPRE.SV40 (Addgene, catalog no. 105545-AAV9).

Viral vectors

Mouse *Mfn1,Mfn2* complementary DNAs (obtained from Addgene plasmids #23212 and #23213, respectively) were tagged at its C terminus with a V5 sequence (GKPIPNPLLGLDST) and fused in-frame to mCherry via a T2A sequence. The Grx1-roGFP2 was a gift from T. P. Dick, DFKZ (Deutsches Krebsforschungszentrum), Heidelberg. The cassettes were subcloned into a pAAV-CAG-FLEX-tdTomato backbone (Addgene reference #28306) by replacing the tdTomato cassette using conventional cloning methods to generate the pAAV-CAG-FLEX-mCherry-T2A-MFN2-V5, pAAV-CAG-FLEX-mCherry-T2A-MFN1-V5, and pAAV-CAG-FLEX-Grx-roGFP2 vectors. A similar strategy was used to generate the control vector pAAV-CAG-FLEX-mCherry. For generation of the AAV-shPCx construct, a plasmid AAV vector (VectorBuilder, pAAV[shRNA]-CMV-mCherry-U6-mPcx-[shRNA#1]) containing the DNA sequences encoding shRNA targeting mouse PCx (5′ CTTTCGCTCTAAGGTGCTA-AACTCGAGTTTAGCACCTTAGAGCGAAAG 3′) under the control of U6 promoter and mCherry under the control CMV promoter was used. Production of a helper-free AAV vector was performed according to the manufacturer's instructions (Cell Biolabs). Briefly, 293AAV cells were transiently transfected with a transfer plasmid carrying mCherry-T2A-MFN2-V5 (pAAV-CAG-FLEX-mCherry-T2A-MFN2-V5),

mCherry-T2A-MFN1-V5 (pAAV-CAG-FLEX-mCherry-T2A-MFN1-V5), mCherry (pAAV-CAG-FLEX-mCherry), or Grx-roGFP2 (pAAV-CAG-FLEX-Grx-roGFP2) coding genes, along with a packing plasmid encoding the AAV1 capsid proteins and a helper plasmid, using the calcium phosphate method. Crude viral supernatants were obtained via lysing cells in phosphate-buffered saline (PBS) by freeze-thaw cycles in a dry ice/ethanol bath. The AAV vectors were purified by discontinuous iodixanol gradient ultracentrifugation (24 hours at 32,000 rpm and 4°C) and concentrated using Amicon ultra-15 centrifugal filter units. Genomic titers of AAV1-CAG-FLEX-mCherry-T2A-MFN2-V5 [2.9×10^{13} genome copies (GC)/ml], AAV1-CAG-FLEX-mCherry (6.1×10^{12} GC/ml), AAV1-CAG-FLEX-MFN1-V5 (1.9×10^{13} GC/ml), and AAV1-CAG-FLEX-Grx-roGFP2 (8.9×10^{12} GC/ml) were determined by real-time quantitative PCR (qPCR) as previously described (*54*).

Western blot procedures

Primary neurons were scraped off in ice-cold 1× PBS, pelleted, and homogenized in 0.5% Triton X-100/0.5% sodium deoxycholate/PBS lysis buffer containing phosphatase and proteinase inhibitors (Roche). Protein quantification was performed by using a bicinchoninic acid assay (Thermo Fisher Scientific). Proteins were then separated by SDS–polyacrylamide gel electrophoresis and blotted onto polyvinylidene difluoride membranes (GE Healthcare). Blocking of unspecific sites and incubation with primary antibodies (see table S1 for details) were performed in 5% milk in TBST (Tris Buffered Saline with Tween), and washing steps and incubation with secondary antibodies were performed in TBST. Incubation with the primary antibodies was carried out at +4°C overnight. After washing, secondary antibodies were applied for 2 hours at room temperature. Equal loading was confirmed by subsequent incubation of the same blot with an anti–β-actin antibody. Detection was done by conversion to chemiluminescence with enhanced chemiluminescence (GE Healthcare).

Immunocytochemistry of primary cortical neurons

Neurons previously seeded on glass coverslips were fixed at the indicated time points with 4% paraformaldehyde (PFA)/PBS for 10 min at room temperature. The coverslips were first permeabilized with 0.1% Triton X-100/PBS for 5 min at room temperature and incubated overnight at 4°C with primary antibodies (see table S1 for details) in blocking buffer [3% bovine serum albumin (BSA)/PBS]. The following day, coverslips were washed with blocking buffer and incubated with appropriate fluorophore-conjugated secondary antibodies for 2 hours at room temperature; last, samples were extensively washed in PBS, counterstained with 4′,6-diamidino-2-phenylindole (DAPI), and mounted on microscopic slides with Aqua-Poly/Mount.

Mouse surgery

Mice (male and females) were anesthetized via an intraperitoneal injection of ketamine (130 mg/kg) and xylazine (10 mg/kg), were administered subcutaneously with the analgesic carprofen (5 mg/kg), and were placed in a stereotactic apparatus (Kopf) provided with a warm pad. The skull was exposed, and a portion covering the cerebellar cortex corresponding to the vermis (from lambda: caudal 1.8, lateral 1, corresponding to lobules IV and V) was thinned with a dental drill. A bent syringe needle was used to carefully create a small perforation of the skull, avoiding disturbing the underlying vasculature. A finely pulled glass capillary was then slowly inserted through the microperforation (ventral −1.3 to −1 from dura), and 200 to 300 nl of AAV was infused in multiple steps at a low pressure via a manual syringe microinjector (Narishige) during a time window of 10 to 20 min. After infusion, the capillary was left in place for an additional 10 min to allow complete diffusion of the virus. After capillary withdrawal, the skin was sutured carefully to minimize wound inflammation, and animals were allowed to recover. Animals followed a postsurgical regimen with analgesics (carpofen) for a few days, during which physical conditions were carefully monitored before eventually euthanizing them at the described time points. All procedures were conducted in accordance with the European, national, and institutional guidelines and were approved by the Landesamt für Natur, Umwelt und Verbraucherschutz, Nordrhein-Westfalen, Germany.

Immunohistochemistry procedures

Animals were anesthetized with ketamine (100 mg/kg) and xylazine (10 mg/kg) and transcardially perfused first with 0.1 M PBS, followed by 4% PFA in PBS. Tissues were dissected and postfixed in 4% PFA/PBS overnight at 4°C. Sagittal sections (50 μm thick) were prepared in PBS from fixed brains using a vibratome (Leica Microsystems GmbH, Vienna, Austria). Staining of free-floating slices was performed at room temperature and under agitation as previously described (*13*), unless otherwise stated. Briefly, the obtained slices were first permeabilized with 0.5% Triton X-100/PBS for 15 min at room temperature; for some epitopes (Pcx and Shmt2), this step was replaced by heating the slices in tris-EDTA buffer (pH 9) for 25 min at 80°C. Next, slices were incubated overnight at 4°C under agitation with the primary antibodies (see table S1 for details) in blocking buffer (3% BSA/PBS). The following day, sections were washed with blocking buffer and incubated with the appropriate fluorophore-conjugated secondary antibodies for 2 hours at room temperature; last, slices were extensively washed in PBS, counterstained with DAPI, and mounted on microscopic slides with AquaPolymount.

Confocal microscopy

Samples were imaged with a laser scanning confocal microscope (TCS SP8-X or TCS Digital Light Sheet, Leica Microsystems) equipped with a white light laser and a 405-diode ultraviolet laser. Stack images in accordance with the Nyquist sampling were acquired with the LAS-X software in sequential mode by exciting the fluorophores and collecting their signal with hybrid detectors (HyDs): For nonquantitative panels, a highly dynamic signal (e.g., mtYFP in soma versus dendrites of PNs) was detected with HyDs in BrightR mode. Gating between 0.3 and 6 ns was applied to reduce background.

Live imaging of sorted cells

Cells were seeded immediately after sorting in Neurobasal-A medium containing 1% B27 supplement and 0.5 mM GlutaMax on poly-L-lysine–coated chamber slides (μ-Slide 8 Well, Ibidi, catalog no. 80826) and then maintained at 37°C and 5% CO_2 for 1 hour to allow cells to settle down. Live imaging was performed on a Leica SP8 laser scanning confocal microscope equipped with a white light laser, HyDs, 63× [1.4 numerical aperture (NA)] oil objective, and a heating stage.

Preparation of acute brain slices

Mice were quickly anesthetized with carbon dioxide and decapitated, and the brain was rapidly removed from the skull and cut into 200-μm-thick (for ^{13}C-labeling experiments) or 275-μm-thick (for

two-photon experiments) sagittal slices by using a vibratome (HM-650 V, Thermo Fisher Scientific, Walldorf, Germany) filled with ice-cold, carbogen-saturated (95% O_2 and 5% CO_2) low-Ca^{2+} artificial cerebrospinal fluid (ACSF) containing the following: 125 mM NaCl, 2.5 mM KCl, 1.25 mM sodium phosphate buffer, 25 mM $NaHCO_3$, 25 mM glucose, 0.5 mM $CaCl_2$, and 3.5 mM $MgCl_2$ (osmolarity of 310 to 330 milliosmoles). The obtained brain slices were transferred into a preincubation chamber containing higher-Ca^{2+} ACSF (125.0 mM NaCl, 2.5 mM KCl, 1.25 mM sodium phosphate buffer, 25.0 mM $NaHCO_3$, 25.0 mM D-glucose, 1.0 mM $CaCl_2$, and 2.0 mM $MgCl_2$, adjusted to pH 7.4 and 310 to 320 milliosmoles).

Two-photon imaging in acute slices

During imaging, slices were moved in a dedicated imaging chamber, and experiments were conducted under continuous ACSF perfusion at a constant temperature of 32° to 33°C. Imaging in slices was performed using a multiphoton laser scanning microscope (TCS SP8 MP-OPO, Leica Microsystems) equipped with a Leica 25× objective (NA 0.95, water), a Ti:Sapphire laser (Chameleon Vision II, Coherent), and a FLIM module (PicoHarp300, PicoQuant).

FLIM of Grx1-roGFP2

Changes in the cytosolic redox state of PNs were measured by two-photon FLIM in sagittal brain slices with targeted expression of the Grx1-roGFP2 biosensor to PNs. Fields of acquisition were selected in the PN layer at about 50 to 80 μm below the surface of the slice for the presence of viable PNs (i.e., lack of beaded structures along dendrites or altered neuronal morphologies) and for the double positivity of PNs to both the roGFP2 sensor and the AAV encoding for shRNA PCx or its control scramble (each coexpressing mCherry). Single-stack images were collected at 512 × 512 pixels with a digital zoom of 2× [excitation wavelength: 890 nm; detection: internal HyD, fluorescein isothiocyanate (FITC) filter set], and image averaging over the course of 2 to 3 min was used to ensure the collection of enough photons (total count of 1000 photons) for curve fitting. Sensitivity of the Grx1-roGFP2 probe and validation of FLIM conditions were carried out by monitoring lifetime values of roGFP2 upon addition of exogenous 10 mM H_2O_2 to the perfusion ACSF (to maximize oxidation, which led to increase of lifetimes), followed by addition of 2 mM dithiothreitol (to maximize reduction, which led to reduction of lifetimes) (fig. S8, D to G). The resulting acquisitions were analyzed using the FLIMfit 5.1.1 software by fitting mono-exponential decay curves of whole images to a measured IRF (instrument response function) with χ^2 approximating 1. To calculate lifetimes of individual PNs, a mask around the neuronal soma was manually drawn, and the average lifetime within each mask was used for quantifications.

Mitochondrial potential analysis

Changes in mitochondrial potential of PNs were measured by two-photon microscopy after 30 min of incubation of acute slices with 100 nM TMRM directly added to the perfusion ACSF. TMRM imaging was performed by exciting the probe at 920 nm, and the signal was acquired with an internal HyD (tetramethyl rhodamine isothiocyanate: 585/40 nm); imaging of mtYFP was performed by using the same excitation wavelength but using a distinct internal HyD (FITC: 525/50). Analysis of mitochondrial potential was assessed at a single-cell level using the Image Calculator plugin from ImageJ. Briefly, the area of mitochondria showing TMRM signal in Purkinje somata was identified in single-stack confocal images of the corresponding channel by using the plugin equation: signal = min (mtYFP, TMRM). The pixel area in the resulting mask was then quantified and subsequently normalized over the corresponding thresholded single-stack image of the mtYFP channel to obtain the fraction of mitochondria displaying mitochondrial potential.

Image processing and representation

Images were deconvolved with the Huygens software (Huygens Pro, Scientific Volume Imaging). For tile scan pictures, a montage of single tiles was made by using the auto-stitching algorithm provided by the LAS-X software. Upon image calibration, ImageJ and Adobe Photoshop were used to further process images and uniformly adjust brightness and contrast. Figure preparation was performed with Adobe Illustrator.

Imaging analyses

mtDNA foci analysis

The number of mtDNA foci was quantified by confocal microscopy on cerebellar sections labeled with an antibody against DNA. Individual regions of interest were created for both the cell body and the nucleus of each cell, and the respective area was calculated with the Multi Measure plugin (ImageJ software). The nuclear area was subtracted from the cell body area to obtain the cytoplasmic area. Last, cytoplasmic DNA puncta indicative of mtDNA were automatically quantified on thresholded pictures by using the Analyze Particles plugin (ImageJ software), and the obtained results were normalized over the average value in PNs from CTRL mice. Results were expressed as mean number of nucleoids per cell.

Protein expression analyses

Protein expression in PNs was assessed at a single-cell level using the Image Calculator plugin from ImageJ. Briefly, the area of mitochondria showing immunoreactivity for a certain antibody in Purkinje somata was identified in single-stack confocal images of the corresponding channel by using the equation: signal = min (mtYFP, antibody). The pixel area in the resulting mask was then quantified and subsequently normalized over the corresponding thresholded single-stack image of the mtYFP channel to obtain the fraction of mitochondria displaying protein.

Purkinje cell density analysis

Purkinje density was assessed with the Cell Counter plugin from ImageJ by dividing the number of counted Purkinje cell by the length of the cerebellar loop occupied by the counted cells.

Transmission electron microscopy procedures

Sample preparation and acquisition

Brains from control and Mfn2cKO mice were fixed with 2% PFA/2.5% glutaraldehyde in 0.1 M phosphate buffer (PB), and then coronal sections (50 to 60 μm thick) were prepared using the vibratome (Leica Mikrosysteme GmbH, Vienna, Austria) and postfixed in 1% osmium tetroxide and 1.5% potassium ferrocyanide in PB buffer for 1 hour at room temperature. Sections were washed three times with distilled water and then stained with 70% ethanol containing 1% uranyl acetate for 20 min. Sections were then dehydrated in graded alcohols and embedded in Durcupan ACM (Araldite casting resin M) epoxy resin (Electron Microscopy Sciences, catalog no. 14040) between silicon-coated glass slides and lastly polymerized for 48 hours at 60°C in an oven. Pieces of cerebellar cortical regions were selected, and ultrathin sections of 50 nm were cut on a Leica Ultracut (Leica Mikrosysteme GmbH, Vienna, Austria) and picked up on a copper slot grid 2 × 1 mm coated with a polystyrene film. Sections

were poststained with 4% uranyl acetate in H_2O for 10 min, rinsed several times with H_2O followed by Reynolds lead citrate in H_2O for 10 min, and rinsed several times with H_2O. Micrographs were taken with a transmission electron microscope Philips CM100 (Thermo Fisher Scientific, Waltham, MA, USA) at an acceleration voltage of 80 kV with a TVIPS (Tietz Video and Image Processing Systems) TemCam-F416 digital camera (TVIPS GmbH, Gauting, Germany).

For mice infected with AAVs, the brain was isolated and cut into 1-mm-thick sagittal sections, and the cerebellum was inspected using a fluorescence microscope for identification of the loops infected by the AAV (i.e., expressing mCherry). Only experiments in which AAV injection resulted in very high efficiency of transduction of the Purkinje cell layer (i.e., nearly the whole layer) in at least two contiguous cerebellar loops were used. AAV-transduced loops were microdissected for overnight postfixation (4% PFA and 2.5% glutaraldehyde in 0.1 M cacodylate buffer) and further processing. For EPON embedding, the fixed tissue was washed with 0.1 M sodium cacodylate buffer (Applichem), incubated with 2% OsO_4 (osmium, Science Services; Caco) in 0.1 M cacodylate buffer (Applichem) for 2 hours at 4°C, and washed again three times with 0.1 M cacodylate buffer. Subsequently, tissue was dehydrated using an ascending ethanol series with 15 min incubation at 4°C in each ethanol solution. Tissues were transferred to propylene oxide and incubated in EPON (Sigma-Aldrich) overnight at 4°C. Tissues were placed in fresh EPON at room temperature for 2 hours, followed by embedding for 72 hours at 62°C. Ultrathin sections of 70 nm were cut using an ultramicrotome (Leica Microsystems, UC6) with a diamond knife (Diatome, Biel, Switzerland) and stained with 1.5% uranyl acetate at 37°C for 15 min and lead citrate solution for 4 min. Electron micrographs were taken with a JEM-2100 Plus Transmission Electron Microscope (JEOL) equipped with a Camera OneView 4K 16 bit (Gatan) and DigitalMicrograph software (Gatan). For analysis, electron micrographs were acquired with a digital zoom of 5000× or 10,000×.

Morphological analyses of mitochondria

For all analyses, ImageJ software was used to manually outline individual mitochondria in the digital images. Different morphological parameters were analyzed. Mitochondrial density was expressed as a percentage calculated by dividing the total mitochondria area per cell by the cytoplasm area (cytoplasm area = cell area − nucleus area) × 100. Mitochondrial circularity was calculated with the formula $[4\pi \cdot (\text{area}/\text{perimeter}^2)]$. Mitochondrial cristae morphology was analyzed and classified into two categories ("tubular" and "vesicular") based on their predominant shape.

Analyses of autophagosome/lysosome number and density

ImageJ software was used to manually outline individual autophagosome/lysosome in the digital images. Autophagosome/lysosome area was expressed as a percentage calculated by dividing the total autophagosome/lysosome structure area per cell by the cytoplasm area (cytoplasm area = cell area − nucleus area) × 100. The density of autophagosome/lysosome was calculated by dividing the total number of autophagosome/lysosome structures per cell by the cytoplasm area (cytoplasm area = cell area − nucleus area).

^{13}C labeling in acute brain slices and isotope enrichment analysis

Labeling of acute slices and sample preparation

For experiments requiring glucose labeling, acute brain slices were transferred into a preincubation chamber containing carbogen-saturated (95% O_2 and 5% CO_2), higher-Ca^{2+} ACSF (125.0 mM NaCl, 2.5 mM KCl, 1.25 mM sodium phosphate buffer, 25.0 mM $NaHCO_3$, 25.0 mM D-glucose, 1.0 mM $CaCl_2$, and 2.0 mM $MgCl_2$, adjusted to pH 7.4 and 310 to 320 mOsm), in which glucose was replaced with $^{13}C_6$-glucose (Eurisotop, catalog no. CLM-1396). For experiments requiring pyruvate labeling, acute brain slices were transferred into a preincubation chamber containing higher-Ca^{2+} ACSF (125.0 mM NaCl, 2.5 mM KCl, 1.25 mM sodium phosphate buffer, 25.0 mM $NaHCO_3$, 25.0 mM D-glucose, 1.0 mM $CaCl_2$, and 2.0 mM $MgCl_2$, adjusted to pH 7.4 and 310 to 320 mOsm), and 1 mM 1-[1-^{13}C]pyruvate was added (Eurisotop, catalog no. CLM-1082). Slices were incubated for 90 min at 37°C. At the end of the experiment, slices were quickly washed with a solution containing 75 mM ammonium carbonate in water (pH 7.4) and then homogenized in 40:40:20 (v:v:v) acetonitrile (ACN):methanol:water. After incubating the slices for 30 min on ice, the samples were centrifuged for 10 min at 21,000*g* at 4°C, and the cleared supernatants were dried down in a SpeedVac concentrator. The resulting dried metabolite pellets were stored at −80°C until analysis.

Liquid chromatography–mass spectrometry analysis of ^{13}C-labeled amino acids

For liquid chromatography–mass spectrometry (LC-MS) analysis, the metabolite pellet was resuspended in 75 µl of LC-MS–grade water (Honeywell). After a 5-min centrifugation at 21,000*g* at 4°C, 20 µl of the cleared supernatant was used for the flux analysis of amino acids, while the remainder of the extract was immediately used for the analysis of anions (see below). Amino acid analysis was performed using a previously described benzoyl chloride derivatization protocol (*55*, *56*). In the first step, 10 µl of 100 mM sodium carbonate (Sigma-Aldrich) was added to the 20 µl of metabolite extract, followed by the addition of 10 µl of 2% benzoylchloride (Sigma-Aldrich) in LC-grade ACN. The samples were briefly vortexed before centrifuging them for 5 min at 21,000*g* at 20°C. The cleared supernatants were transferred to 2-ml autosampler vials containing conical glass inserts (200 µl volume). Samples were analyzed using an Acquity iClass Ultra-Performance LC system (Waters) connected to a Q-Exactive (QE)–HF (ultra-high-field Orbitrap) high-resolution accurate mass spectrometer (Thermo Fisher Scientific). For the analysis, 2 µl of the derivatized sample was injected onto a 100 × 1.0 mm High Strength Silica T3 column (Waters), packed with 1.8-µm particles. The flow rate was 100 µl/min, and the buffer system consisted of buffer A (10 mM ammonium formate and 0.15% formic acid in water) and buffer B (ACN). The gradient was as follows: 0% B at 0 min; 0 to 15% B at 0 to 0.1 min; 15 to 17% B at 0.1 to 0.5 min; 17 to 55% B at 0.5 to 14 min; 55 to 70% B at 14 to 14.5 min; 70 to 100% B at 14.5 to 18 min; 100% B at 18 to 19 min; 100 to 0% B at 19 to 19.1 min; 0% B at 19.1 to 28 min (*55*, *56*). The QE-HF mass spectrometer was operating in positive ionization mode monitoring in the mass range *m/z* (mass/charge ratio) 50 to 750. The applied resolution was 60,000, with an acquired gain control (AGC) ion target of 3×10^6 and a maximal ion time of 100 ms. The heated electrospray ionization (ESI) source was operating with a spray voltage of 3.5 kV, a capillary temperature of 250°C, a sheath gas flow of 60 AU (arbitrary units), and an auxiliary gas flow of 20 AU at a temperature of 250°C. The S-lens was set to 60 AU.

Anion chromatography–MS analysis of ^{13}C-labeled organic acids

The remainder (55 µl) of the resuspended metabolite pellet was analyzed using a Dionex ion chromatography system (ICS 5000+, Thermo Fisher Scientific) connected to the QE-HF mass spectrometer

(Thermo Fisher Scientific). In brief, 5 µl of the metabolite extract was injected in push partial-loop mode using an overfill factor of 1 onto a Dionex IonPac AS11-HC column (2 mm by 250 mm, 4 µm particle size, Thermo Fisher Scientific) equipped with a Dionex IonPac AG11-HC guard column (2 mm by 50 mm, 4 µm, Thermo Fisher Scientific). The column temperature was held at 30°C, while the autosampler was set to 6°C. A potassium hydroxide gradient was generated by an eluent generator using a potassium hydroxide cartridge that was supplied with deionized water. The metabolite separation was carried out at a flow rate of 380 µl/min, applying the following gradient: 0 to 3 min, 10 mM KOH; 3 to 12 min, 10 to 50 mM KOH; 12 to 19 min, 50 to 100 mM KOH; 19 to 21 min, 100 mM KOH; 21 to 21.5 min, 100 to 10 mM KOH. The column was reequilibrated at 10 mM KOH for 8.5 min.

The eluting metabolites were merged post-column with a make-up flow of 150 µl/min of isopropanol before directing the flow to the high-resolution mass spectrometer operating in negative ionization mode. The MS was monitoring a mass range of m/z 50 to 750 at a resolution of 60,000. AGC was set to a value of 1×10^6, and the maximum ion time was held at 100 ms. The heated ESI source was operating with a spray voltage of 3.5 kV. Further settings of the ion source were as follows: capillary temperature, 275°C; sheath gas flow, 60 AU; auxiliary gas flow, 20 AU at 300°C, while the S-lens was set to 60 AU.

Data analysis of ^{13}C-labeled metabolites

Data analysis of isotope ratios was performed using the TraceFinder software (Version 4.2, Thermo Fisher Scientific). The identity of each compound was validated by authentic reference compounds, which were analyzed independently. For the isotope enrichment analysis, the area of the extracted ion chromatogram (XIC) of each ^{13}C isotope (M_n), where n is the number of carbons of the target compound, was extracted from the $[M + H]^+$ for the analysis of amino acids or $[M - H]^+$ for the analysis of anions. XICs were determined with a mass accuracy <5 parts per million and an RT precision of 0.05 min. Enrichment analysis was performed by calculating the proportions of each detected isotope toward the sum of all isotopes of the corresponding compound. These proportions are given as percent values for each isotope, and results are indicated as molar percent enrichment (M.P.E.) as previously described (*42*).

Metabolomic analysis of sorted neurons

Frozen neuronal pellets were homogenized in ice-cold 80% methanol (v/v), vortexed, and incubated for 30 min at −20°C. Samples were vortexed once more and put under agitation for 30 min at +4°C. Samples were centrifuged for 5 min at 21,000*g* at 4°C, and the resulting supernatants were collected and dried with the SpeedVac concentrator at 25°C for subsequent analysis. LC-MS analysis of amino acids of the sorted cells was performed as described above. Data analysis was performed using the monoisotopic mass of each compound using TraceFinder (Version 4.2, Thermo Fisher Scientific). Metabolite data were quantile-normalized using the preprocessCore package (*57*).

Electrophysiology

Slice preparation

Mice were quickly anesthetized with carbon dioxide and decapitated, and the brain was rapidly removed from the skull and cut into sagittal slices of 300 to 375 µm by using the vibratome (HM-650 V, Thermo Fisher Scientific, Walldorf, Germany) filled with ice-cold, carbogenated (95% O_2 and 5% CO_2) low-Ca^{2+} ACSF (125.0 mM NaCl, 2.5 mM KCl, 1.25 mM sodium phosphate buffer, 25.0 mM $NaHCO_3$, 25.0 mM D-glucose, 1.0 mM $CaCl_2$, and 6.0 mM $MgCl_2$, adjusted to pH 7.4 and 310 to 330 mOsm). The obtained brain slices were transferred into a chamber containing higher-Ca^{2+} ACSF (125.0 mM NaCl, 2.5 mM KCl, 1.25 mM sodium phosphate buffer, 25.0 mM $NaHCO_3$, 25.0 mM D-glucose, 4.0 mM $CaCl_2$, and mM 3.5 $MgCl_2$, adjusted to pH 7.4 and 310 to 320 mOsm). Slices were stored for 20 to 30 min to allow recovery before performing recordings.

Recording

All recordings were performed using a microscope stage equipped with a fixed recording chamber and a 20× water-immersion objective (Scientifica). Putative Purkinje cells were identified by (i) soma size, (ii) anatomical localization in the cerebellum, and (iii) the expression of the fluorescent mtYFP reporter. Patch pipettes with a tip resistance of 5 to 11 megohms were made from borosilicate glass capillary tubing (GB150-10, 0.86 mm × 1.5 mm × 100 mm, Science Products, Hofheim, Germany) with a horizontal pipette puller (P-1000, Sutter Instruments, Novato, CA). All recordings were performed with an ELC-03XS npi patch-clamp amplifier (npi electronic GmbH, Tamm, Germany) that was controlled by the software Signal (version 6.0, Cambridge Electronic, Cambridge, UK). The experiments were recorded with a sampling rate of 12.5 kHz. The signal was filtered with two short-pass Bessel filters that had cutoff frequencies of 1.3 and 10 kHz. Capacitance of the membrane and pipette was compensated by using the compensation circuit of the amplifier. All experiments were performed under visual control using an Orca-Flash 4.0 camera (Hamamatsu, Geldern, Germany) controlled by the software Hokawo (version 2.8, Hamamatsu, Geldern, Germany).

Conventional whole-cell configuration and analysis

Immediately before recording, the patch pipette was filled with internal solution containing the following: 4.0 mM KCl, 2.0 mM NaCl, 0.2 mM EGTA, 135.0 mM K-gluconate, 10.0 mM Hepes, 4.0 mM ATP(Mg), 0.5 mM guanosine triphosphate (GTP) (Na), and 10.0 mM phosphocreatin, adjusted to pH 7.25 and osmolarity 290 mOsm (sucrose). Resting membrane potential was instantly measured after rupturing the membrane while applying 0 pA. Input resistance was measured by applying hyperpolarizing current injections of −40, −30, −20, and −10 pA. The amplitude of the voltage response was measured, and input resistance was calculated using Ohm's law. Spontaneous activity was recorded for 5 min in voltage clamp, while sPSCs were identified and measured using a semiautomatic identification script in Igor Pro (version 32 7.01, WaveMetrics, Lake Oswego, OR, USA). *I-V* curves and steady-state currents were measured by clamping the cells at different potentials, starting from −110 mV, and by increasing the voltage with steps of 5 mV. Generation of APs was tested by applying depolarizing current injections. Cells were clamped at −70 mV, while depolarizing current pulses were applied. Step sizes were adjusted to each recorded cell individually (10 to 60 pA). Maximum AP frequency was calculated by manually counting spikes of a pulse that elicited the highest AP frequency. AP threshold was analyzed by using the second differentiation of a depolarizing pulse that elicited for the first time one or more APs.

Perforated patch configuration and analysis

Perforated patch recordings were performed using standard protocols. Recordings were performed with ATP- and GTP-free pipette solution containing the following: 128 mM K-gluconate, 10 mM KCl, 10 mM Hepes, 0.1 mM EGTA, and 2 mM $MgCl_2$ and adjusted

to pH 7.2 (with KOH). ATP and GTP were omitted from the intracellular solution to prevent uncontrolled permeabilization of the cell membrane. The patch pipette was filled with amphotericin-containing internal solution (~200 to 250 μg/ml; G4888, Sigma-Aldrich) to achieve perforated patch recordings. Amphotericin was dissolved in dimethyl sulfoxide (final concentration: 0.1 to 0.3%; DMSO; D8418, Sigma-Aldrich). The used DMSO concentration had no obvious effect on the investigated neurons. During the perforation process, access resistance (Ra) was constantly monitored, and experiments were started after Ra and the AP amplitude were stable (20 to 40 min). Spontaneous activity was measured for 2 to 5 min in voltage and/or current clamp. Data analysis was performed with Igor Pro (version 7.05.2, WaveMetrics, USA), Excel (version 2010, Microsoft Corporation, Redmond, USA), and GraphPad Prism (version 8.1.2, GraphPad Software Inc., La Jolla, CA, USA). To identify spontaneous APs, the NeuroMatic v3.0c plugin for IgorPro was used. APs were automatically identified with a given threshold that was individually adapted for each recording. Using the interspike intervals, the interspike frequency with maximum instantspike frequency and average spike frequency were determined.

Flow cytometry of PNs

PNs isolation

PNs were purified from mouse cerebella at the indicated stages by adapting a previously published protocol (*58*). Briefly, cerebella were dissected and chopped in ice-cold dissociation medium [HBSS Ca^{2+}- and Mg^{2+}-free, supplemented with 20 mM glucose, penicillin (50 U/ml), and streptomycin (0.05 mg/ml)] and then digested in papain medium [HBSS, supplemented with L-cysteine·HCl (1 mg/ml), papain (16 U/ml), and deoxyribonuclease I (DNase I; 0.1 mg/ml)] at 37°C for 30 min. Tissues were first washed in HBSS medium containing ovomucoid (10 mg/ml), BSA (10 mg/ml), and DNase (0.1 mg/ml) at room temperature to block the enzymatic digestion and then gently triturated in HBSS containing 20 mM glucose, penicillin (50 U/ml), streptomycin (0.05 mg/ml), and DNase (0.1 mg/ml) to release single cells. The resulting cell suspension was filtered through a 70-μm cell strainer, and then cells were pelleted by centrifugation (1110 rpm, 5 min, 4°C) and resuspended in sorting medium [HBSS, supplemented with 20 mM glucose, 20% fetal bovine serum, penicillin (50 U/ml), and streptomycin (0.05 mg/ml)]; cell viability was assessed by using propidium iodide, and cell density was adjusted to 1×10^6 to 2×10^6 cells/ml; the suspension was filtered through a 50-μm cell strainer before flow cytometry.

Flow cytometry

Cell sorting was performed at 4°C using a FACSAria III machine (BD Biosciences) with FACSDiva software (BD Biosciences, version 8.0.1). Cell suspension was sorted using a 100-μm nozzle at 20 psi pressure at a rate of ~2800 events/s. Since the traditional gating criteria (cell size, doublet discrimination, and scatter properties) could not ensure a proper separation of PNs from the other cell types, the gating strategy was set based on a direct comparison of YFP intensity versus autofluorescence in mitoYFP+ and control mitoYFP− mice. YFP was excited by illuminating the sample with a 488-nm laser line, and the signal was detected using a 530/30-nm band-pass filter. The relative intensity of the Rosa26-mitoYFP reporter in mitoYFP+ mice was also used to discriminate neuronal somata from axonal debris. 7-AAD was excited with a 561-nm yellow laser and detected using a 675/20-nm band-pass filter to exclude dead cells. For simultaneous isolation of astrocytes, cell suspension was stained with ACSA-2-APC, and then the sample was illuminated with a 640-nm laser line, and the signal was detected using a 660/20-nm band-pass filter.

Collected cells were then pelleted by centrifugation (1110 rpm, 5 min, 4°C) and stored at −80°C until use. Mfn2cKO mice and their control littermates were sorted on the same day to minimize procedural variability. FACS data presentation and analysis were performed using the FlowJo software (FlowJo LLC, Ashland, OR, USA).

Isolation of DNA and mtDNA quantification in sorted neurons

DNA isolation for subsequent mtDNA quantification from sorted neurons was performed by real-time PCR as previously described (*59*). Linearity and threshold sensitivity were initially tested by running the qPCR with different amounts of cells. Briefly, 300 PNs were collected in lysis buffer consisting of 50 mM tris-HCl (pH 8.5), 1 mM EDTA, 0.5% Tween 20, and proteinase K (200 ng/ml) and incubated at 55°C for 120 min. Further incubation of the cells at 95°C for 10 min ensured complete inactivation of proteinase K. mtDNA was measured by semiquantitative PCR in a 7900HT Real-Time PCR System (Thermo Fisher Scientific) using TaqMan probes specific for the mt-Nd1 (Thermo Fisher Scientific, catalog no. Mm04225274_s1), mt-Nd6 (Thermo Fisher Scientific, catalog no. AIVI3E8), and 18*S* (Thermo Fisher Scientific, catalog no. Hs99999901_s1) genes.

Proteomic analysis of sorted neurons and astrocytes

Proteomic sample preparation

Frozen neuronal pellets were lysed in lysis buffer [6 M guanidinium chloride, 10 mM tris(2-carboxyethyl)phosphine hydrochloride, 10 mM chloroacetamide, and 100 mM tris-HCl] by heating the solution at 95°C for 10 min and sonicating it for 10 min (30-s pulse/30-s pause cycles) on Bioruptor (Diagenode). Samples were diluted 1:10 in 20 mM tris-HCl (pH 8.0) and mixed with 300 ng of Trypsin Gold (Promega) and incubated overnight at 37°C to achieve complete digestion. On the following day, samples were centrifuged for 20 min at 20,000*g*. The supernatant was diluted with 0.1% formic acid, and the solution was desalted using homemade StageTips. Samples were dried in a SpeedVac apparatus (Eppendorf concentrator plus 5305) at 45°C, and the peptides were suspended with 0.1% formic acid. All samples were prepared at the same time by the same person. For the analysis of the astrocyte samples, 4 μg of desalted peptides was labeled with tandem mass tags (TMT10plex, catalog no. 90110, Thermo Fisher Scientific) using a 1:20 ratio of peptides to TMT reagent. For TMT labeling, 0.8 mg of TMT reagent was resuspended with 70 μl of anhydrous ACN, and dried peptides were reconstituted in 9 μl of 0.1 M TEAB (Triethylammonium bicarbonate), to which 7 μl of TMT reagent in ACN was added to a final ACN concentration of 43.75%, and after 60 min of incubation, the reaction was quenched with 2 μl of 5% hydroxylamine. Labeled peptides were pooled, dried, resuspended in 200 μl of 0.1% formic acid (FA), split into two, and desalted using homemade StageTips. One of the two halves was fractionated on a 1-mm by 150-mm Acquity column, packed with 130-Å, 1.7-μm C18 particles (Waters, catalog no. SKU: 186006935), using an UltiMate 3000 Ultrahigh-performance LC (Thermo Fisher Scientific). Peptides were separated at a flow of 30 μl/min, with a 96-min segmented gradient from 1 to 50% buffer B for 85 min and from 50 to 95% buffer B for 3 min, followed by 8 min of 95% buffer B; buffer A was 5% ACN and 10 mM ammonium bicarbonate (ABC), and buffer B was 80% ACN and 10 mM ABC. Fractions were collected every 3 min,

and fractions were pooled into two groups (1 + 17, 2 + 18, etc.), and dried in a vacuum centrifuge.

LC-MS/MS analysis

For MS analysis, peptides were separated on a 25-cm, 75-μm–internal diameter PicoFrit analytical column (New Objective, part no. PF7508250) packed with 1.9-μm ReproSil-Pur 120 C18-AQ media (Dr. Maisch, mat. no. r119.aq) using an EASY-nLC 1200 (Thermo Fisher Scientific, Germany). The column was maintained at 50°C. Buffers A and B were 0.1% formic acid in water and 0.1% formic acid in 80% ACN, respectively. Peptides were separated on a segmented gradient from 6 to 31% buffer B for 65 min and from 31 to 50% buffer B for 5 min at 200 nl/min. Eluting peptides were analyzed on an Orbitrap Fusion mass spectrometer (Thermo Fisher Scientific). Peptide precursor *m/z* measurements were carried out at 120,000 resolution in the 350 to 1500 *m/z* range. The most intense precursors with charge state from 2 to 6 only were selected for Higher-energy C-trap Dissociation (HCD) fragmentation using 27% normalized collision energy. The cycle time was set to 1 s. The *m/z* values of the peptide fragments were measured in the ion trap using a minimum AGC target of 5×10^4 and 86 ms maximum injection time. Upon fragmentation, precursors were put on a dynamic exclusion list for 45 s. TMT-labeled peptides were separated on a 50-cm, 75-μm Acclaim PepMap column (Thermo Fisher Scientific, catalog no. 164942) and analyzed on an Orbitrap Lumos Tribrid mass spectrometer (Thermo Fisher Scientific) equipped with a High Field Asymmetric Waveform Ion Mobility Spectrometry (FAIMS) device (Thermo Fisher Scientific) that was operated in two compensation voltages, −50 and −70 V. Synchronous precursor selection–based MS3 was used for TMT reporter ion signal measurements. Peptide separations were performed on the EASY-nLC 1200 using a 90-min linear gradient from 6 to 31% buffer; buffer A was 0.1% FA, and buffer B was 0.1% FA and 80% ACN. The analytical column was operated at 50°C. Raw files were split on the basis of the FAIMS compensation voltage using FreeStyle (version 1.6, Thermo Fisher Scientific).

Protein identification and quantification

The raw data were analyzed with MaxQuant version 1.5.2.8 (https://maxquant.org/) using the integrated Andromeda search engine. Peptide fragmentation spectra were searched against the canonical and isoform sequences of the mouse reference proteome (proteome ID UP000000589, downloaded in May 2017 from UniProt) in addition to the sequences of Cre recombinase and YFP from *Aequorea victoria*. Methionine oxidation and protein N-terminal acetylation were set as variable modifications; cysteine carbamidomethylation was set as a fixed modification. The digestion parameters were set to "specific" and "Trypsin/P." The minimum number of peptides and razor peptides for protein identification was 1; the minimum number of unique peptides was 0. Protein identification was performed at peptide spectrum matches and a protein false discovery rate of 0.01. The "second peptide" option was on. Successful identifications were transferred between the different raw files using the "match between runs" option. Label-free quantification (LFQ) (*60*) was performed using an LFQ minimum ratio count of 1. LFQ intensities were filtered for at least two valid values in at least one genotype group per time point and imputed from a normal distribution with a width of 0.3 and down shift of 1.8. Analysis of the LFQ results was performed with the Perseus computation platform (https://maxquant.net/perseus/) and R (https://r-project.org/). Differential expression analysis was performed using a two-sided moderated *t* test from the limma package (*61*). Exploratory data analysis was performed using ggplot, FactoMineR, factoextra, GGally, and pheatmap. TMT-based proteomics data were analyzed using MaxQuant version 1.6.10.43. Raw proteomics data were searched against the human proteome database from UniProt, downloaded in September 2018. The isotope purity correction factors, provided by the manufacturer, were included in the analysis. Differential expression analysis was performed using limma in R. The raw data, database search results, and the data analysis workflow and results were deposited to the ProteomeXchange Consortium via the PRIDE partner repository with the dataset identifier PXD019690.

Functional annotation enrichment analysis

The Ingenuity Pathway Analysis (QIAGEN) tool was used to determine the enrichment of functional annotation terms for the dataset at 8 weeks (Fig. 1). Briefly, the list of quantified proteins obtained from the LC-MS/MS (tandem mass spectrometry) data analysis was used with the following filtering criteria: *Mus musculus* was selected as species and background, and categories showing a Benjamini adjusted *P* value for enrichment of 0.05 or lower were considered significant. For the figure, the top five overrepresented categories in each cluster, based on the adjusted *P* value, are shown. Time-course protein expression analysis of significant candidates identified in each category was performed using a multiple *t* test with a two-stage linear step-up procedure of Benjamini, Krieger, and Yekutieli, with $Q = 5\%$, and each row was analyzed individually, without assuming a consistent SD.

To compare the results in this study to published databases and generate the Venn diagrams in Fig. 1, we combined our list of quantified proteins with annotations from MitoCarta 2.0 (*24*). Diagrams were generated using the online tool Draw Venn Diagram (http://bioinformatics.psb.ugent.be/webtools/Venn/).

Statistical analysis

Details of statistical procedures used for the proteomic analyses are available in the corresponding section of Materials and Methods. For all the other experiments, details can be found in the corresponding figure legend. Unless otherwise stated, all data are presented as means ± SEM, and all statistical analyses were performed using GraphPad Prism 8.1.2 software.

SUPPLEMENTARY MATERIALS

Supplementary material for this article is available at http://advances.sciencemag.org/cgi/content/full/6/35/eaba8271/DC1

View/request a protocol for this paper from *Bio-protocol*.

REFERENCES AND NOTES

1. C. M. Gustafsson, M. Falkenberg, N.-G. Larsson, Maintenance and expression of mammalian mitochondrial DNA. *Annu. Rev. Biochem.* **85**, 133–160 (2016).
2. A. Suomalainen, B. J. Battersby, Mitochondrial diseases: The contribution of organelle stress responses to pathology. *Nat. Rev. Mol. Cell Biol.* **19**, 77–92 (2018).
3. H. Chen, M. Vermulst, Y. E. Wang, A. Chomyn, T. A. Prolla, J. M. McCaffery, D. C. Chan, Mitochondrial fusion is required for mtDNA stability in skeletal muscle and tolerance of mtDNA mutations. *Cell* **141**, 280–289 (2010).
4. E. Silva Ramos, E. Motori, C. Brüser, I. Kühl, A. Yeroslaviz, B. Ruzzenente, J. H. K. Kauppila, J. D. Busch, K. Hultenby, B. H. Habermann, S. Jakobs, N.-G. Larsson, A. Mourier, Mitochondrial fusion is required for regulation of mitochondrial DNA replication. *PLOS Genet.* **15**, e1008085 (2019).
5. J. Nikkanen, S. Forsström, L. Euro, I. Paetau, R. A. Kohnz, L. Wang, D. Chilov, J. Viinamäki, A. Roivainen, P. Marjamäki, H. Liljenbäck, S. Ahola, J. Buzkova, M. Terzioglu, N. A. Khan, S. Pirnes-Karhu, A. Paetau, T. Lönnqvist, A. Sajantila, P. Isohanni, H. Tyynismaa, D. K. Nomura, B. J. Battersby, V. Velagapudi, C. J. Carroll, A. Suomalainen, Mitochondrial

DNA replication defects disturb cellular dNTP pools and remodel one-carbon metabolism. *Cell Metab.* **23**, 635–648 (2016).
6. N. A. Khan, J. Nikkanen, S. Yatsuga, C. Jackson, L. Wang, S. Pradhan, R. Kivela, A. Pessia, V. Velagapudi, A. Suomalainen, mTORC1 regulates mitochondrial integrated stress response and mitochondrial myopathy progression. *Cell Metab.* **26**, 419–428.e5 (2017).
7. I. Kühl, M. Miranda, I. Atanassov, I. Kuznetsova, Y. Hinze, A. Mourier, A. Filipovska, N.-G. Larsson, Transcriptomic and proteomic landscape of mitochondrial dysfunction reveals secondary coenzyme Q deficiency in mammals. *eLife* **6**, e30952 (2017).
8. V. Carelli, D. C. Chan, Mitochondrial DNA: Impacting central and peripheral nervous systems. *Neuron* **84**, 1126–1142 (2014).
9. G. Pfeffer, R. Horvath, T. Klopstock, V. K. Mootha, A. Suomalainen, S. Koene, M. Hirano, M. Zeviani, L. A. Bindoff, P. Yu-Wai-Man, M. Hanna, V. Carelli, R. McFarland, K. Majamaa, D. M. Turnbull, J. Smeitink, P. F. Chinnery, New treatments for mitochondrial disease—No time to drop our standards. *Nat. Rev. Neurol.* **9**, 474–481 (2013).
10. B. H. Goodpaster, L. M. Sparks, Metabolic flexibility in health and disease. *Cell Metab.* **25**, 1027–1036 (2017).
11. M. Bélanger, I. Allaman, P. J. Magistretti, Brain energy metabolism: Focus on astrocyte-neuron metabolic cooperation. *Cell Metab.* **14**, 724–738 (2011).
12. U. Fünfschilling, L. M. Supplie, D. Mahad, S. Boretius, A. S. Saab, J. Edgar, B. G. Brinkmann, C. M. Kassmann, I. D. Tzvetanova, W. Möbius, F. Diaz, D. Meijer, U. Suter, B. Hamprecht, M. W. Sereda, C. T. Moraes, J. Frahm, S. Goebbels, K.-A. Nave, Glycolytic oligodendrocytes maintain myelin and long-term axonal integrity. *Nature* **485**, 517–521 (2012).
13. E. Motori, J. Puyal, N. Toni, A. Ghanem, C. Angeloni, M. Malaguti, G. Cantelli-Forti, B. Berninger, K.-K. Conzelmann, M. Götz, K. F. Winklhofer, S. Hrelia, M. Bergami, Inflammation-induced alteration of astrocyte mitochondrial dynamics requires autophagy for mitochondrial network maintenance. *Cell Metab.* **18**, 844–859 (2013).
14. A. A. Polyzos, D. Y. Lee, R. Datta, M. Hauser, H. Budworth, A. Holt, S. Mihalik, P. Goldschmidt, K. Frankel, K. Trego, M. J. Bennett, J. Vockley, K. Xu, E. Gratton, C. T. McMurray, Metabolic reprogramming in astrocytes distinguishes region-specific neuronal susceptibility in huntington mice. *Cell Metab.* **29**, 1258–1273.e11 (2019).
15. S. Züchner, I. V. Mersiyanova, M. Muglia, N. Bissar-Tadmouri, J. Rochelle, E. L. Dadali, M. Zappia, E. Nelis, A. Patitucci, J. Senderek, Y. Parman, O. Evgrafov, P. De Jonghe, Y. Takahashi, S. Tsuji, M. A. Pericak-Vance, A. Quattrone, E. Battologlu, A. V. Polyakov, V. Timmerman, J. M. Schröder, J. M. Vance, Mutations in the mitochondrial GTPase mitofusin 2 cause Charcot-Marie-Tooth neuropathy type 2A. *Nat. Genet.* **36**, 449–451 (2004).
16. H. Chen, J. M. McCaffery, D. C. Chan, Mitochondrial fusion protects against neurodegeneration in the cerebellum. *Cell* **130**, 548–562 (2007).
17. A. L. Misko, Y. Sasaki, E. Tuck, J. Milbrandt, R. H. Baloh, Mitofusin2 mutations disrupt axonal mitochondrial positioning and promote axon degeneration. *J. Neurosci.* **32**, 4145–4155 (2012).
18. S. Lee, F. H. Sterky, A. Mourier, M. Terzioglu, S. Cullheim, L. Olson, N.-G. Larsson, Mitofusin 2 is necessary for striatal axonal projections of midbrain dopamine neurons. *Hum. Mol. Genet.* **21**, 4827–4835 (2012).
19. A. H. Pham, S. Meng, Q. N. Chu, D. C. Chan, Loss of *Mfn2* results in progressive, retrograde degeneration of dopaminergic neurons in the nigrostriatal circuit. *Hum. Mol. Genet.* **21**, 4817–4826 (2012).
20. F. H. Sterky, S. Lee, R. Wibom, L. Olson, N.-G. Larsson, Impaired mitochondrial transport and Parkin-independent degeneration of respiratory chain-deficient dopamine neurons in vivo. *Proc. Natl. Acad. Sci. U.S.A.* **108**, 12937–12942 (2011).
21. A. Kratz, P. Beguin, M. Kaneko, T. Chimura, A. M. Suzuki, A. Matsunaga, S. Kato, N. Bertin, T. Lassmann, R. Vigot, P. Carninci, C. Plessy, T. Launey, Digital expression profiling of the compartmentalized translatome of Purkinje neurons. *Genome Res.* **24**, 1396–1410 (2014).
22. J. P. Doyle, J. D. Dougherty, M. Heiman, E. F. Schmidt, T. R. Stevens, G. Ma, S. Bupp, P. Shrestha, R. D. Shah, M. L. Doughty, S. Gong, P. Greengard, N. Heintz, Application of a translational profiling approach for the comparative analysis of CNS cell types. *Cell* **135**, 749–762 (2008).
23. J. J. Barski, K. Dethleffsen, M. Meyer, Cre recombinase expression in cerebellar Purkinje cells. *Genesis* **28**, 93–98 (2000).
24. S. E. Calvo, K. R. Clauser, V. K. Mootha, MitoCarta2.0: An updated inventory of mammalian mitochondrial proteins. *Nucleic Acids Res.* **44**, D1251–D1257 (2016).
25. L. R. Molnar, K. A. Thayne, W. W. Fleming, D. A. Taylor, The role of the sodium pump in the developmental regulation of membrane electrical properties of cerebellar Purkinje neurons of the rat. *Brain Res. Dev. Brain Res.* **112**, 287–291 (1999).
26. M. Yudkoff, Interactions in the metabolism of glutamate and the branched-chain amino acids and ketoacids in the CNS. *Neurochem. Res.* **42**, 10–18 (2017).
27. A. Daemen, B. Liu, K. Song, M. Kwong, M. Gao, R. Hong, M. Nannini, D. Peterson, B. M. Liederer, C. de la Cruz, D. Sangaraju, A. Jaochico, X. Zhao, W. Sandoval, T. Hunsaker, R. Firestein, S. Latham, D. Sampath, M. Evangelista, G. Hatzivassiliou, Pan-cancer metabolic signature predicts co-dependency on glutaminase and de novo glutathione synthesis linked to a high-mesenchymal cell state. *Cell Metab.* **28**, 383–399.e9 (2018).
28. M. F. Utter, D. B. Keech, Pyruvate carboxylase. I. Nature of the reaction. *J. Biol. Chem.* **238**, 2603–2608 (1963).
29. A. C. H. Yu, J. Drejer, L. Hertz, A. Schousboe, Pyruvate carboxylase activity in primary cultures of astrocytes and neurons. *J. Neurochem.* **41**, 1484–1487 (1983).
30. H. Waelsch, S. Berl, C. A. Rossi, D. D. Clarke, D. P. Purpura, Quantitative aspects of CO_2 fixation in mammalian brain in vivo. *J. Neurochem.* **11**, 717–728 (1964).
31. M. I. Ekstrand, M. Terzioglu, D. Galter, S. Zhu, C. Hofstetter, E. Lindqvist, S. Thams, A. Bergstrand, F. S. Hansson, A. Trifunovic, B. Hoffer, S. Cullheim, A. H. Mohammed, L. Olson, N.-G. Larsson, Progressive parkinsonism in mice with respiratory-chain-deficient dopamine neurons. *Proc. Natl. Acad. Sci. U.S.A.* **104**, 1325–1330 (2007).
32. M. C. McKenna, J. H. Stevenson, X. Huang, J. T. Tildon, C. L. Zielke, I. B. Hopkins, Mitochondrial malic enzyme activity is much higher in mitochondria from cortical synaptic terminals compared with mitochondria from primary cultures of cortical neurons or cerebellar granule cells. *Neurochem. Int.* **36**, 451–459 (2000).
33. R. Vogel, G. Jennemann, J. Seitz, H. Wiesinger, B. Hamprecht, Mitochondrial malic enzyme: Purification from bovine brain, generation of an antiserum, and immunocytochemical localization in neurons of rat brain. *J. Neurochem.* **71**, 844–852 (1998).
34. B. Hassel, A. Bråthe, Neuronal pyruvate carboxylation supports formation of transmitter glutamate. *J. Neurosci.* **20**, 1342–1347 (2000).
35. G. Bukato, Z. Kochan, J. Swierczynski, Subregional and intracellular distribution of NADP-linked malic enzyme in human brain. *Biochem. Med. Metab. Biol.* **51**, 43–50 (1994).
36. L. R. Gray, S. C. Tompkins, E. B. Taylor, Regulation of pyruvate metabolism and human disease. *Cell. Mol. Life Sci.* **71**, 2577–2604 (2014).
37. M. S. Patel, L. G. Korotchkina, Regulation of the pyruvate dehydrogenase complex. *Biochem. Soc. Trans.* **34**, 217–222 (2006).
38. M. Gutscher, A.-L. Pauleau, L. Marty, T. Brach, G. H. Wabnitz, Y. Samstag, A. J. Meyer, T. P. Dick, Real-time imaging of the intracellular glutathione redox potential. *Nat. Methods* **5**, 553–559 (2008).
39. R. J. DeBerardinis, A. Mancuso, E. Daikhin, I. Nissim, M. Yudkoff, S. Wehrli, C. B. Thompson, Beyond aerobic glycolysis: Transformed cells can engage in glutamine metabolism that exceeds the requirement for protein and nucleotide synthesis. *Proc. Natl. Acad. Sci. U.S.A.* **104**, 19345–19350 (2007).
40. A. R. Mullen, W. W. Wheaton, E. S. Jin, P.-H. Chen, L. B. Sullivan, T. Cheng, Y. Yang, W. M. Linehan, N. S. Chandel, R. J. DeBerardinis, Reductive carboxylation supports growth in tumour cells with defective mitochondria. *Nature* **481**, 385–388 (2011).
41. Q. Chen, K. Kirk, Y. I. Shurubor, D. Zhao, A. J. Arreguin, I. Shahi, F. Valsecchi, G. Primiano, E. L. Calder, V. Carelli, T. T. Denton, M. F. Beal, S. S. Gross, G. Manfredi, M. D'Aurelio, Rewiring of glutamine metabolism is a bioenergetic adaptation of human cells with mitochondrial DNA mutations. *Cell Metab.* **27**, 1007–1025.e5 (2018).
42. A. S. Divakaruni, M. Wallace, C. Buren, K. Martyniuk, A. Y. Andreyev, E. Li, J. A. Fields, T. Cordes, I. J. Reynolds, B. L. Bloodgood, L. A. Raymond, C. M. Metallo, A. N. Murphy, Inhibition of the mitochondrial pyruvate carrier protects from excitotoxic neuronal death. *J. Cell Biol.* **216**, 1091–1105 (2017).
43. H. S. Waagepetersen, H. Qu, A. Schousboe, U. Sonnewald, Elucidation of the quantitative significance of pyruvate carboxylation in cultured cerebellar neurons and astrocytes. *J. Neurosci. Res.* **66**, 763–770 (2001).
44. A. J. Sweatt, M. A. Garcia-Espinosa, R. Wallin, S. M. Hutson, Branched-chain amino acids and neurotransmitter metabolism: Expression of cytosolic branched-chain aminotransferase (BCATc) in the cerebellum and hippocampus. *J. Comp. Neurol.* **477**, 360–370 (2004).
45. L. B. Sullivan, D. Y. Gui, A. M. Hosios, L. N. Bush, E. Freinkman, M. G. Vander Heiden, Supporting aspartate biosynthesis is an essential function of respiration in proliferating cells. *Cell* **162**, 552–563 (2015).
46. T. Klockgether, C. Mariotti, H. L. Paulson, Spinocerebellar ataxia. *Nat. Rev. Dis. Primers.* **5**, 24 (2019).
47. E. R. Almajan, R. Richter, L. Paeger, P. Martinelli, E. Barth, T. Decker, N.-G. Larsson, P. Kloppenburg, T. Langer, E. I. Rugarli, AFG3L2 supports mitochondrial protein synthesis and Purkinje cell survival. *J. Clin. Invest.* **122**, 4048–4058 (2012).
48. Y. Kageyama, Z. Zhang, R. Roda, M. Fukaya, J. Wakabayashi, N. Wakabayashi, T. W. Kensler, P. H. Reddy, M. Iijima, H. Sesaki, Mitochondrial division ensures the survival of postmitotic neurons by suppressing oxidative damage. *J. Cell Biol.* **197**, 535–551 (2012).
49. M. Ripolone, V. Lucchini, D. Ronchi, G. Fagiolari, A. Bordoni, F. Fortunato, S. Mondello, S. Bonato, M. Meregalli, Y. Torrente, S. Corti, G. P. Comi, M. Moggio, M. Sciacco, Purkinje cell COX deficiency and mtDNA depletion in an animal model of spinocerebellar ataxia type 1. *J. Neurosci. Res.* **96**, 1576–1585 (2018).
50. D. M. Stucki, C. Ruegsegger, S. Steiner, J. Radecke, M. P. Murphy, B. Zuber, S. Saxena, Mitochondrial impairments contribute to Spinocerebellar ataxia type 1 progression and can be ameliorated by the mitochondria-targeted antioxidant MitoQ. *Free Radic. Biol. Med.* **97**, 427–440 (2016).

51. K. Sharma, S. Schmitt, C. G. Bergner, S. Tyanova, N. Kannaiyan, N. Manrique-Hoyos, K. Kongi, L. Cantuti, U.-K. Hanisch, M. A. Philips, M. J. Rossner, M. Mann, M. Simons, Cell type– and brain region–resolved mouse brain proteome. *Nat. Neurosci.* **18**, 1819–1831 (2015).
52. E. C. Bayraktar, L. Baudrier, C. Özerdem, C. A. Lewis, S. H. Chan, T. Kunchok, M. Abu-Remaileh, A. L. Cangelosi, D. M. Sabatini, K. Birsoy, W. W. Chen, MITO-Tag mice enable rapid isolation and multimodal profiling of mitochondria from specific cell types in vivo. *Proc. Natl. Acad. Sci. U.S.A.* **116**, 303–312 (2019).
53. C. Fecher, L. Trovò, S. A. Müller, N. Snaidero, J. Wettmarshausen, S. Heink, O. Ortiz, I. Wagner, R. Kühn, J. Hartmann, R. M. Karl, A. Konnerth, T. Korn, W. Wurst, D. Merkler, S. F. Lichtenthaler, F. Perocchi, T. Misgeld, Cell-type-specific profiling of brain mitochondria reveals functional and molecular diversity. *Nat. Neurosci.* **22**, 1731–1742 (2019).
54. C. Aurnhammer, M. Haase, N. Muether, M. Hausl, C. Rauschhuber, I. Huber, H. Nitschko, U. Busch, A. Sing, A. Ehrhardt, A. Baiker, Universal real-time PCR for the detection and quantification of adeno-associated virus serotype 2-derived inverted terminal repeat sequences. *Hum. Gene Ther. Methods* **23**, 18–28 (2012).
55. P. A. Malec, M. Oteri, V. Inferrera, F. Cacciola, L. Mondello, R. T. Kennedy, Determination of amines and phenolic acids in wine with benzoyl chloride derivatization and liquid chromatography–mass spectrometry. *J. Chromatogr. A* **1523**, 248–256 (2017).
56. J.-M. Wong, P. A. Malec, O. S. Mabrouk, J. Ro, M. Dus, R. T. Kennedy, Benzoyl chloride derivatization with liquid chromatography–mass spectrometry for targeted metabolomics of neurochemicals in biological samples. *J. Chromatogr. A* **1446**, 78–90 (2016).
57. J. Lee, J. Park, M. S. Lim, S. J. Seong, J. J. Seo, S. M. Park, H. W. Lee, Y.-R. Yoon, Quantile normalization approach for liquid chromatography–mass spectrometry-based metabolomic data from healthy human volunteers. *Anal. Sci.* **28**, 801–805 (2012).
58. L. A. Catapano, M. W. Arnold, F. A. Perez, J. D. Macklis, Specific neurotrophic factors support the survival of cortical projection neurons at distinct stages of development. *J. Neurosci.* **21**, 8863–8872 (2001).
59. R. W. Taylor, M. J. Barron, G. M. Borthwick, A. Gospel, P. F. Chinnery, D. C. Samuels, G. A. Taylor, S. M. Plusa, S. J. Needham, L. C. Greaves, T. B. Kirkwood, D. M. Turnbull, Mitochondrial DNA mutations in human colonic crypt stem cells. *J. Clin. Invest.* **112**, 1351–1360 (2003).
60. J. Cox, M. Y. Hein, C. A. Luber, I. Paron, N. Nagaraj, M. Mann, Accurate proteome-wide label-free quantification by delayed normalization and maximal peptide ratio extraction, termed MaxLFQ. *Mol. Cell. Proteomics* **13**, 2513–2526 (2014).
61. M. E. Ritchie, B. Phipson, D. Wu, Y. Hu, C. W. Law, W. Shi, G. K. Smyth, *limma* powers differential expression analyses for RNA-sequencing and microarray studies. *Nucleic Acids Res.* **43**, e47 (2015).

Acknowledgments: We wish to thank A. Taha, T. Örztürk, and J. Daraspe for the excellent technical assistance; P. Pelzer for providing the scripts used to analyze electrophysiological recordings; M. Jevtic for support with viral vector design; M. Bergami for support with animal licenses; Y. Hinze and S. Perin for technical support with the metabolite measurements; A.-L. Schumacher and the other members of the FACS & Imaging Core Facility for assistance with FACS experiments; the Comparative Biology Facility for maintaining mouse colonies at the Max Planck Institute for Biology of Ageing; the Electron Microscopy Facility at the University of Lausanne and the CECAD Imaging Facility in Cologne for the use of electron microscopes; and D. A. Giunta for help with graphical illustration of proposed model. **Funding:** This work was supported by the Deutsche Forschungsgemeinschaft (SFB1218, Advanced Postdoc Grant) to E.M.; the Swiss National Science Foundation to N.T.; by the Swiss National Foundation (310030_163064 and 310030_182332) to J.P.; and by the Swedish Research Council (2015-00418), the Knut and Alice Wallenberg Foundation, and the European Research Council (Advanced Grant 2016-741366) to N.-G.L. **Author contributions:** E.M. and N.-G.L. conceived the study and wrote the manuscript. E.M. designed the cell isolation protocol, carried out protein data annotation and interpretation, performed most of the experiments, analyzed data, and prepared figures. I.A. performed MS and data analysis. K.F.-D. assisted with FACS and contributed to the interpretation of flow cytometry data. J.P. and N.T. generated and analyzed electron microscopy data. S.M.V.K. performed and analyzed electrophysiological recordings. V.S. generated viral vectors. P.G. performed metabolomics analysis. All authors discussed the data and critically revised the manuscript. **Competing interests:** The authors declare that they have no competing interests. **Data and materials availability:** All data needed to evaluate the conclusions in the paper are present in the paper and/or the Supplementary Materials. Proteomics data are available via ProteomeXchange with identifier PXD019690. Additional data related to this paper may be requested from the corresponding authors.

Submitted 9 January 2020
Accepted 15 July 2020
Published 28 August 2020
10.1126/sciadv.aba8271

Citation: E. Motori, I. Atanassov, S. M. V. Kochan, K. Folz-Donahue, V. Sakthivelu, P. Giavalisco, N. Toni, J. Puyal, N.-G. Larsson, Neuronal metabolic rewiring promotes resilience to neurodegeneration caused by mitochondrial dysfunction. *Sci. Adv.* **6**, eaba8271 (2020).